the exponential factor in equation 4.2, where factors other than E_t do not contribute significantly to the temperature dependence. Since the temperature dependence of E_t is dominated by the bandgap temperature dependence, the same is expected for the temperature dependence of the tunneling current, resulting in a concave shape of tunneling current vs. temperature on a linear scale, as seen in Fig. 4.6a. When plotted on a logarithmic scale, the tunneling current is expected to have the following form:

$$\log I_t \propto E_t \propto E_G \tag{4.4}$$

If instead of temperature, the corresponding bandgap is used as x-axis and the tunneling current is plotted on a logarithmic scale, a linear dependence vs. bandgap is expected resulting from the linear dependence on E_t (equation 4.4). This is shown in Fig. 4.6b. We have assumed that the $Si_{1-x}Ge_x$ bandgap has the same temperature dependence as that of Si (given in ref. [86]), i.e. that the $Si/Si_{1-x}Ge_x$ bandgap offset (105meV for x=0.15) is temperature independent. The same method to identify excess tunneling current was used in ref. [81].

4.3 Discussion

For the same n-type doping, the tunneling currents in our devices are approximately three orders of magnitude lower than those of the ion implanted devices previously reported [78]. If the implanted junctions were somewhat compensated due to the non-abrupt implantation profiles, the actual junction doping would be less than indicated, making the RTCVD results even better in comparison. Since the tunneling current is mediated by midgap states at the junction, the vast reduction in tunneling currents of the devices fabricated by RTCVD implies a commensurate reduction of density of defects at the interface. This may be due to the absence of residual implant-related damage in the RTCVD junctions, and these results indicate high quality of epitaxial

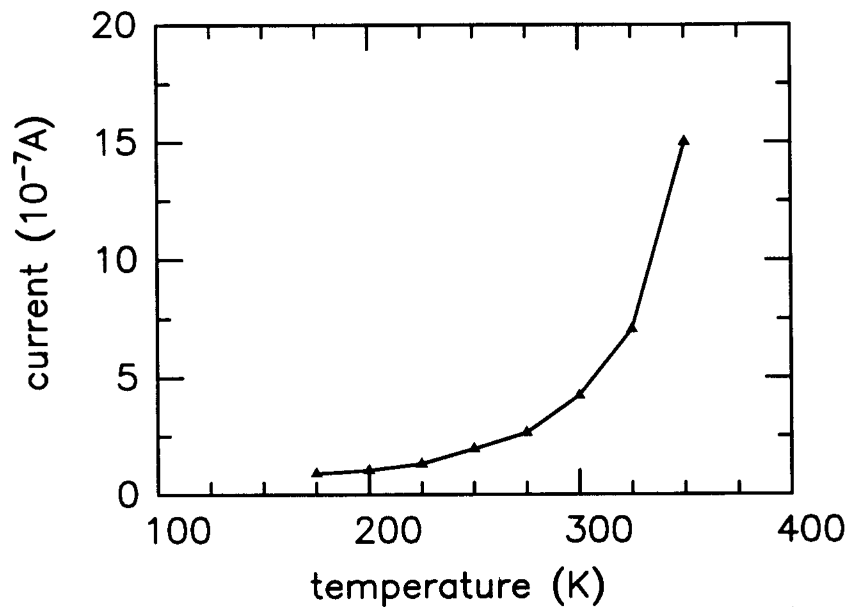

a)

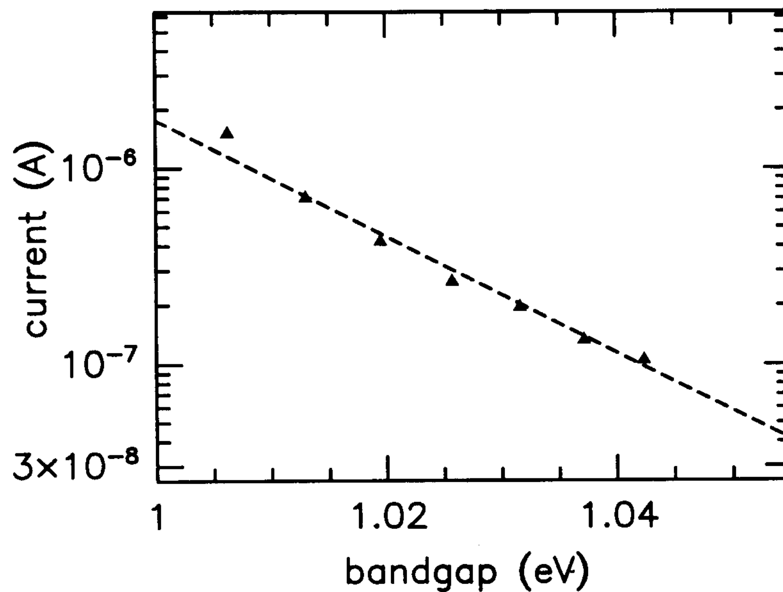

b)

Figure 4.6: a) Typical current vs. temperature dependence of a heavily doped SiGe/Si device ($N_D = 1 \times 10^{19}$ cm^{-3}, $V_a = 0.32$V, $A = 3.25 \times 10^{-4}$ cm^2). b) Current vs. $Si_{0.85}Ge_{0.15}$ bandgap of the same device. The data confirms the expected shape of excess tunneling current.

interfaces. We have no independent measurement of the midgap state densities at the junction to confirm this hypothesis, however. Base-emitter junctions are often formed by diffusion from doped polysilicon instead of ion implantation in present-day technology. Significant tunneling currents have also been observed in base-emitter junctions formed by a poly-Si emitter process [80, 81], but no systematic data on tunneling current densities as the function of doping at the junction, like that of [78], has been reported.

The implications of these results for HBT performance are shown in Fig. 4.7. It is shown how the tunneling current is predicted to limit the current gain in a $Si/Si_{0.85}Ge_{0.15}/Si$ HBT with a base doping 5×10^{19} cm^{-3} and a basewidth of 500Å, as the emitter doping is increased. Without the presence of tunneling, the gain would follow the ideal curve shown in the figure. At higher emitter doping levels, the ideal curve bends due to the bandgap narrowing in the heavily doped silicon emitter. The minority carrier parameters of del Alamo [84] are used to model n-Si emitter. With tunneling, the gain curves are predicted to drop rapidly after a certain doping is reached since tunneling causes a significant increase in the base current. The effects of the tunneling levels in epitaxially grown junctions are contrasted to those in implanted junctions, previously reported. The reduction in parasitic tunneling current at the same doping level that we observed predicts a shift towards higher emitter doping and an increase in the peak gain. The low tunneling current enables high gain to be maintained to higher base doping levels, enabling reduced base resistances and increased Early voltages.

To avoid excess tunneling currents, often proposed device structures have a reduced emitter doping at the base-emitter junction or a lighter doped emitter spacer layer [87]. However, the lighter doped (1×10^{18} cm^{-3} or less) emitter layer could lead to a degradation of high speed performance due to an increase in the emitter storage time, normally negligible in heavily doped emitters [47].

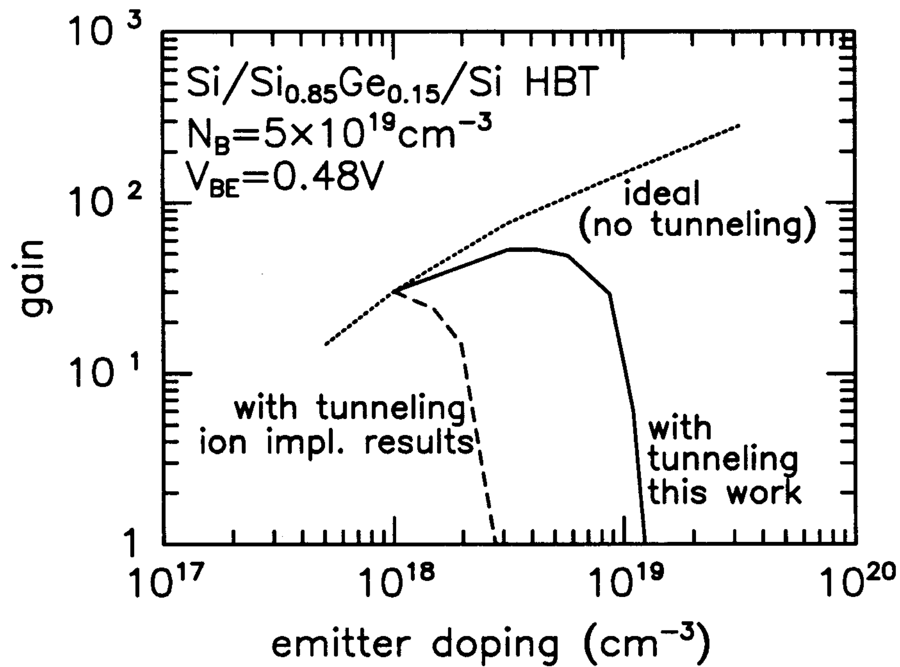

Figure 4.7: Calculated effects of the tunneling current on the gain of $Si/Si_{1-x}Ge_x/Si$ HBT's as the emitter doping is increased. Both curves based on the ion implantation results and this data are given for comparison, as well as the ideal curve (no tunneling).

4.4 Conclusions

A reduction of three orders of magnitude in forward bias tunneling current densities of RTCVD fabricated Si/Si and Si/SiGe junctions compared to ion implanted results is observed. These results demonstrate the high quality of the epitaxial interface, i.e. lower interface states densities compared to ion-implanted junctions. Low tunneling currents allow higher limits to transistor base and emitter dopings which imply higher gains, reduced base resistances and higher Early voltages of scaled devices. The results imply an upper limit of doping at the base-emitter interface of 1×10^{19} cm^{-3} before a substantial degradation of base current in $Si/Si_{1-x}Ge_x$ HBT's.

a)

sample number	n-doping from C-V ($10^{18}cm^{-3}$)	n-doping from spreading resistance ($10^{18}cm^{-3}$)	junction
436	2.7	3.5	Si/Si
437	6.2	7.7	Si/Si
438	8.5	9.5	Si/Si
466	0.13	-	Si/Si
467	10	12	Si/SiGe
468	1.5	-	Si/SiGe
469	1.5	-	Si/Si

b)

sample number	n-layer growth			p-layer growth		
	temperature (°C)	PH_4 flow (sccm) (70ppm in H_2)	time (min)	temperature (°C)	B_2H_6 flow (sccm) (10ppm in H_2)	time (min)
436	1000	500	6			
	+ 850	10	100			
437	1000	500	60	700	500	50
438	1000	500	6			
438	+ 900	500	95			
466	1000	-	10			
469	1000	20	6			
467	900	500	10	625	200 +48sccm GeH_4	7.5
468	1000	20	6	700	500	50

Table 4.1: Summary of p^+–n^+diodes: a) doping, b) growth parameters

Chapter 5

Lateral Hole and Vertical Electron Currents in $Si_{1-x}Ge_x$ Bases

5.1 Introduction

Although high performance $Si/Si_{1-x}Ge_x/Si$ bipolar devices have been demonstrated, experimental data for even DC modeling of these devices is still lacking. In silicon, it is well known that the heavy doping in the emitter of bipolar transistors causes bandgap narrowing that affects minority carrier transport, namely, the narrower gap in the emitter causes an exponential decrease in collector current (an opposite effect to HBT action). For that reason, heavy doping effects in silicon, particularly in n-type material, have been extensively studied [84, 85, 88, 89].

In $Si/Si_{1-x}Ge_x/Si$ HBT's, the $Si_{1-x}Ge_x$ base is generally heavily doped. The effects of heavy base doping on vertical electron and lateral hole currents have not been substantially experimentally measured, although heavy base doping is often employed in the design of narrow-base devices. Vertical minority carrier transport, crucial for accurate modeling of collector current, is affected by heavy–doping–induced bandgap narrowing while lateral hole current, which is important for base sheet resistance, is affected by hole drift mobility. One needs to study both the effects of Ge and the doping to understand and accurately predict the performance of $Si/Si_{1-x}Ge_x/Si$ HBT's.

In this chapter we present a set of comprehensive measurements of lateral hole current and vertical electron current across the strained $Si_{1-x}Ge_x$ base of an npn HBT in a wide range of base dopings and Ge concentrations. Based on room temperature measurements, we have extracted the effective bandgap for electron transport. We have also developed an empirical model for the collector current enhancement with respect to all-Si devices vs. base sheet resistance.

5.2 Device fabrication

For this study, we fabricated $Si/Si_{1-x}Ge_x/Si$ HBT's with flat Ge and B profiles in the base grown by Rapid Thermal Chemical Vapor Deposition (RTCVD). $Si_{1-x}Ge_x$ layers were grown at 625°C, while Si emitters were grown at 800°C for 7.5 minutes. Base dopings ranged from $10^{18}cm^{-3}$ to $10^{20}cm^{-3}$ and Ge concentrations ranged from 0% to 27%. Base widths varied from 300Å to 2000Å. The devices with more Ge in the base had narrower bases to avoid strain relaxation. The Ge concentrations were measured by x-ray diffraction. The Ge fraction was measured by the shift of the 400 peak (Cu $K\alpha$ radiation line) using: $x = 0.178 \times \Delta(2\theta)$. The estimated error in x is $\pm1\%$. Undoped SiGe base-emitter and base-collector layers, 50Å to 200Å thick were introduced to avoid parasitic barriers due to boron outdiffusion during the emitter growth (see chapter 2). SIMS measurements confirmed flat profiles, base dopings and widths, and that the B-doping was contained within the SiGe layer (Fig. 5.1). The device structure is shown in Fig. 5.2. Van der Pauw patterns for base resistance measurements were made on each sample in addition to transistors.

A simple double mesa wet-etch process without any thermal cycles over 400°C was used to prevent any possibility of parasitic barriers due to the thermal diffusion. No emitter implants were used since these can cause anomalous base dopant diffusion in $Si_{1-x}Ge_x$ HBT's for even moderate temperatures [90] and thus cause parasitic

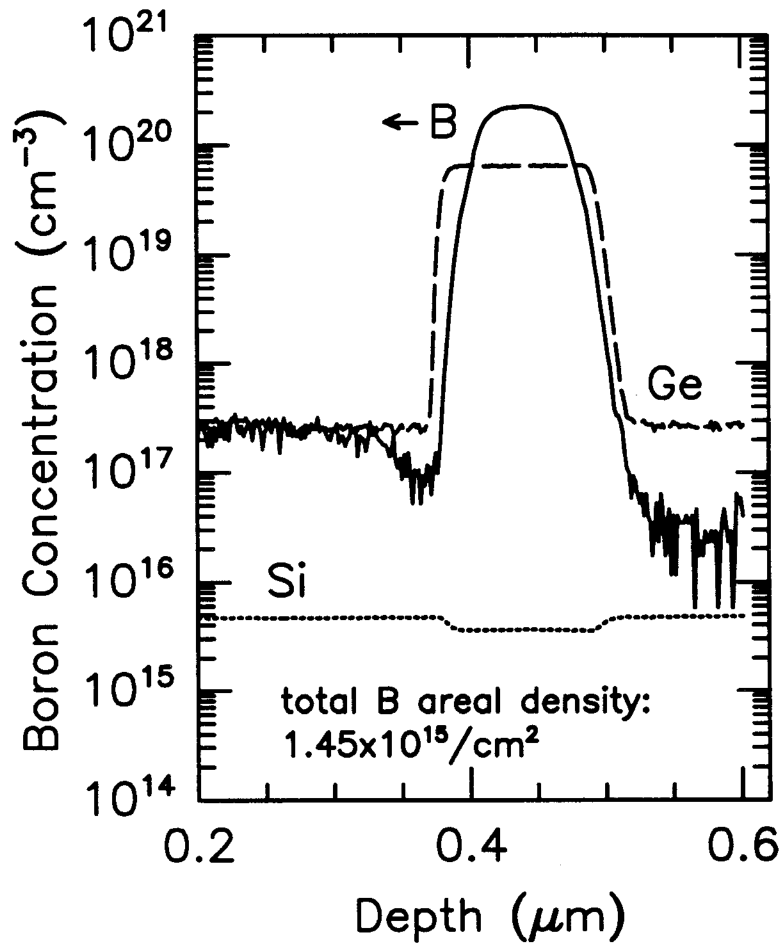

Figure 5.1: A typical SIMS profile of a device used in this study. Si and Ge are in arbitrary units. B was contained within the SiGe layer even for the heaviest doped devices.

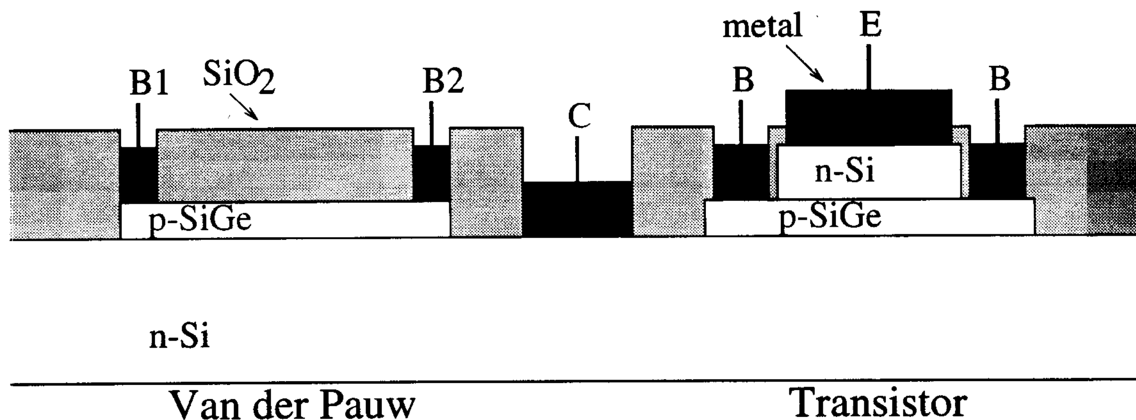

Figure 5.2: A typical device structure used in this study. Van der Pauw patterns were fabricated next to transistor devices.

barriers. A selective wet etch [91] was used to remove the emitter for contacting the base layer. The highest temperature step in the whole process was during the emitter growth. We have done experiments prior to this study to confirm that the $Si_{1-x}Ge_x$ layers were fully strained and no barrier formation occured during the emitter growth (also confirmed by SIMS).

The emitter area of transistors ranged from $20 \times 20\mu m^2$ to $100 \times 100\mu m^2$. No significant perimeter effects in the collector current measurements were observed.

5.3 Majority carrier properties

Lateral hole mobility in p-type heavily doped $Si_{1-x}Ge_x$ is of great importance for accurate modeling of base sheet resistance. The mobility important for base sheet resistance in equation 2.6 is the low field drift mobility. However, the most often measured mobility is the one measured by Hall measurements, i.e. Hall mobility. Drift and Hall mobilities reflect the band structure and scattering mechanism in different ways. They are the same in case of parabolic or spherical energy bands and energy independent carrier scattering times. This is not the case, however, in heavily doped, strained $Si_{1-x}Ge_x$. The ratio of Hall and drift mobility is usually defined as

the Hall scattering factor ($r_H = \mu_{p,Hall}/\mu_{p,drift}$).

The strain affects the band structure in $Si_{1-x}Ge_x$ alloys. The degeneracy of conduction and valence bands is lifted, moving four conduction band minima in the growth plane down with respect to the other two, and splitting heavy and light hole bands with the heavy hole band lying higher. Because of strain-induced changes in the energy bands of $Si_{1-x}Ge_x$ alloys, a reduction in hole effective mass compared to bulk Si is expected [92]. This would tend to cause a higher drift mobility [93, 94]. The effect is expected to be more pronounced in the direction perpendicular to the growth plane. On the other hand, the presence of alloy scattering would tend to reduce the hole mobility. Some experimental evidence exists to support an enhancement in hole drift mobility with increasing Ge concentration at a single doping level [95]. In this work we measured hole Hall mobilities, sheet resistivities, drift mobilities and Hall scattering factors over a wide range of dopings ($10^{18} - 10^{20}cm^{-3}$) and Ge concentrations (0-27%).

Fig. 5.3.a shows the measured Hall mobility ($\mu_{p,Hall}$) of holes at room temperature as a function of base doping. Different symbols represent different Ge concentrations (x). A decrease in the Hall mobility with increasing doping is obvious, as expected due to the increase in ionized impurity scattering. However, for similar doping levels, Hall mobilities decrease with the increasing Ge concentration. This is clearly shown in Fig. 5.3.b where the Hall mobility is plotted vs. Ge concentration for devices with similar doping levels.

The measurement of drift mobility ($\mu_{p,drift}$) and Hall scattering factor requires an independent measurement of carrier concentration in the base, in addition to Hall measurements. The integrated hole concentration was obtained from SIMS profiles, assuming full dopant activation. The SIMS results were calibrated by implanted standards into similar $Si_{1-x}Ge_x$ layers. The results were also corrected for the expected effects of base-emitter and base-collector space-charge regions. The full activation of

a)

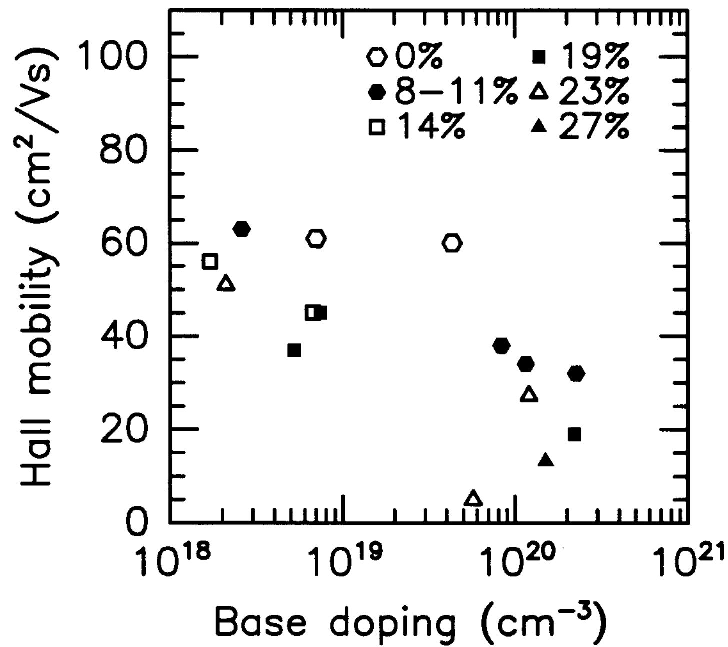

b)

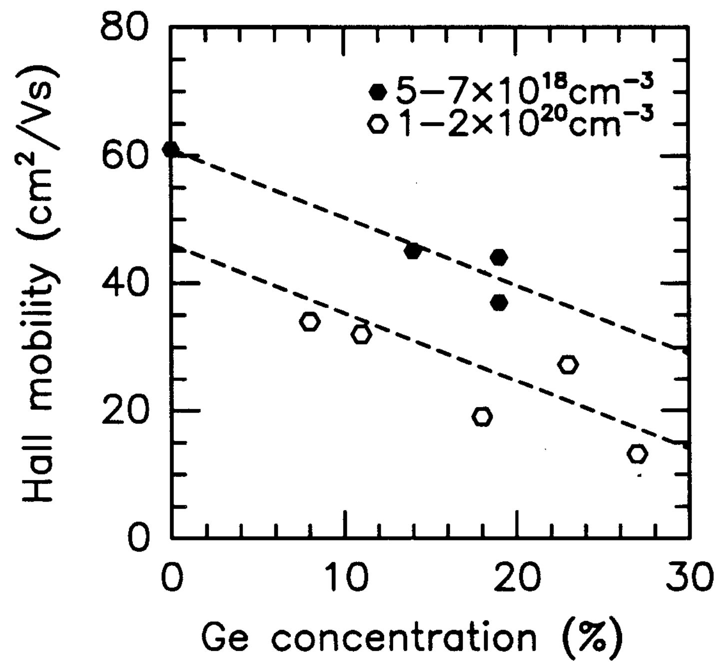

Figure 5.3: a) Hole lateral Hall mobility as a function of base doping for various Ge concentrations, b) Hole lateral Hall mobility as a function of Ge concentration for different doping levels.

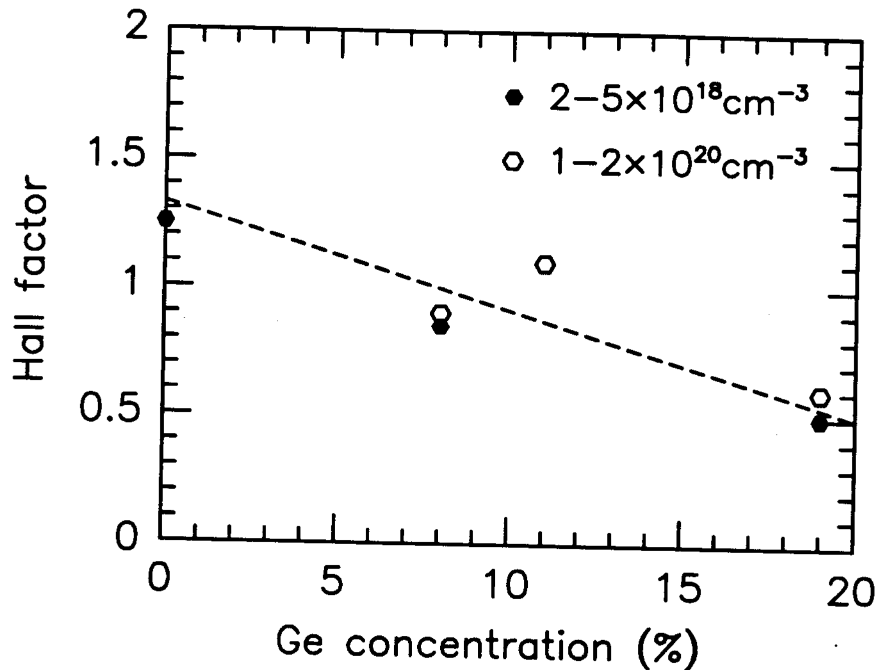

Figure 5.4: Hall scattering factor for holes as a function of Ge concentration

B atoms is a reasonable assumption, since the emitters were grown at 800°C for 7.5 minutes after the in-situ doped $Si_{1-x}Ge_x$ base layers. The accuracy of the extracted values for Hall scattering factor and drift mobility is expected to be ±20%. By comparing the measured integrated hole concentration in the base by Hall measurements to those measured by SIMS, we extracted the Hall scattering factor. Fig. 5.4 shows the Hall scattering factor as a function of x. It is obvious that the Hall scattering factor decreases with increasing Ge content and for $x \geq 0.1$ is actually less than unity. No clear doping dependence of Hall scattering factor was observed. Note that if the hole concentrations were lower than the chemical boron concentrations obtained by SIMS (due to incomplete dopant activation), the resulting Hall scattering factor would be even lower. A similar trend of decreasing Hall scattering factor with increasing Ge concentration was also observed by McGregor et al. [95]. This behaviour is not yet well understood. The difference between Hall and drift mobility depends on the

detailed structure of the valence bands and hole scattering mechanisms which, to the knowledge of the authors, has not been addressed in $Si_{1-x}Ge_x$ strained alloys.

Fig. 5.5.a shows drift mobility as a function of base doping for different Ge concentrations. No clear dependence of drift mobility on Ge concentration was observed, as illustrated in Fig. 5.5.b. Although at dopings of $5-7\times10^{18}\text{cm}^{-3}$ a slight increase with increasing Ge content was noticed, consistent with the results of ref. [95], at high doping levels ($1-2\times10^{20}\text{cm}^{-3}$) no dependence on Ge concentration was observed. For subsequent modeling purposes, a best fit to experimental data is given by:

$$\mu_{P_{drift}} = 20 + \frac{350}{1+(\frac{N_A}{10^{17}\text{cm}^{-3}})^{0.5}} \tag{5.1}$$

This is plotted as a dashed line in Fig. 5.5. Measurement of hole drift mobility in a wide range of doping and Ge concentrations enables the prediction of base sheet resistance for an arbitrary structure.

5.4 Effective bandgap measurements and model

The effect of bandgap narrowing in heavily doped Si, relevant for electrical device performance, is often modeled as an increase in intrinsic effective minority carrier concentration [96, 97]. For a p-type material this would be:

$$n_{i,eff}^2 = n_{io}^2\, e^{\frac{\Delta E_{G,eff}}{k_B T}} \tag{5.2}$$

where $n_{i,eff}$ is the effective intrinsic carrier concentration, n_{io} is the true intrinsic carrier concentration and $\Delta E_{G,eff}$ is the effective (apparent) bandgap narrowing. We have extended this approach to HBT's, where $\Delta E_{G,eff}$ includes bandgap narrowing due to Ge in the base as well as heavy doping.

It is well known that the collector saturation current density of an HBT with flat Ge and doping profiles without parasitic conduction band barriers or spikes due to

a)

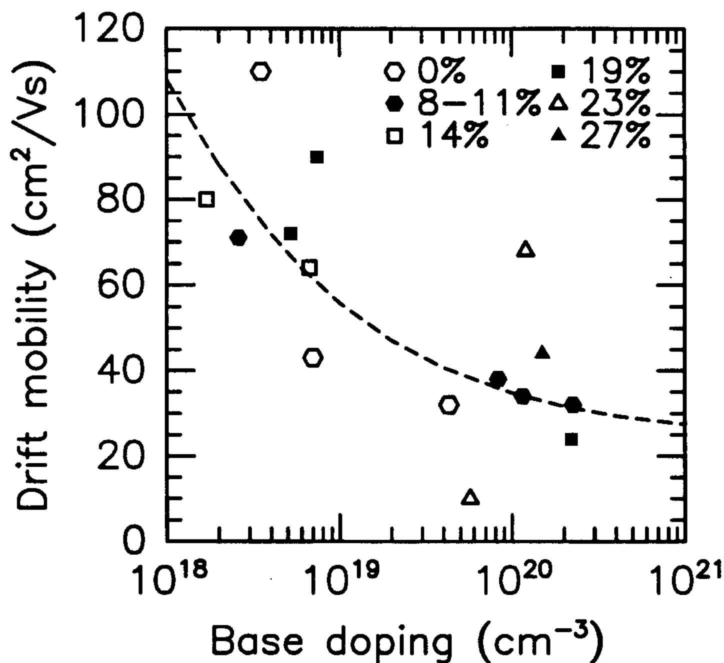

b)

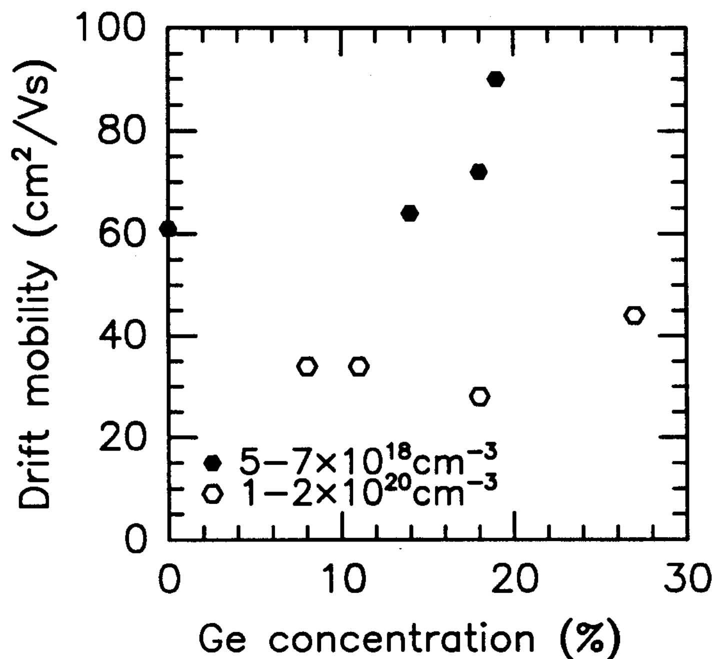

Figure 5.5: a) Drift mobility as a function of base doping for various Ge concentrations. The line is the fit to data, b) Drift mobility as a function of Ge concentrations for two doping levels.

conduction band offsets in the base can be modeled as:

$$J_{co} = \frac{qD_n N_c N_v}{G_B} e^{\frac{-E_{G,eff}}{k_B T}} \tag{5.3}$$

where D_n is the minority carrier diffusion coefficient, N_c and N_v are conduction and valence band densities of states, G_B is the Gummel number in the $Si_{1-x}Ge_x$ base, and $E_{G,eff}$ is the effective bandgap for minority carrier concentration in the base. The effective bandgap is determined by the Ge concentration in $Si_{1-x}Ge_x$, but narrowing due to heavy doping, observed in Si [85] and SiGe [98], should also be taken into account. The equation 5.3 can be rewritten as follows:

$$J_{co} = \frac{qD_{n,SiGe}}{G_{B,SiGe}} \frac{(N_c N_v)_{SiGe}}{(N_c N_v)_{Si}} n_{io,Si}^2 \, e^{\frac{\Delta E_{G,eff}}{k_B T}} \tag{5.4}$$

where $\Delta E_{G,eff}$ is the effective bandgap reduction with respect to intrinsic Si. The ratio $(N_c N_v)_{SiGe}/(N_c N_v)_{Si}$ represents the reduction in densities of states due to strain-induced splitting of the bands in $Si_{1-x}Ge_x$, and all heavy doping effects are included in $\Delta E_{G,eff}$.

Based on equation 5.4 there are two ways in which $\Delta E_{G,eff}$ may be found. The first possibility is to compare J_{CO} of the HBT to that of a similar all-Si device as a function of temperature [14, 99, 100, 18]. If one assumes a similar temperature dependence of mobility, densities of states and bandgap in the $Si_{1-x}Ge_x$ as in Si, one can extract a $\Delta E_{G,eff}$ from the temperature dependence of the ratio of J_{CO} in the two devices. This method has an advantage that no knowledge of electron diffusion coefficient D_n or base doping level is required. However, if one uses a lightly doped Si sample as a reference, one makes an implicit error because of the known difference in the temperature dependence of D_n in p-type Si at different doping levels [101]. For example, from room temperature down to 200K, the ratio of D_n in p-type Si doped $\sim 5 \times 10^{18}$ cm^{-3} to that doped 6×10^{19} cm^{-3} changes from 1.1 to 0.3 [85, 101]. This could introduce an error of $\sim$ 65 meV in $\Delta E_{G,eff}$ if it were extracted from a fit of the

ratio of J_{C0}'s over this same temperature range. This might be overcome if one had all Si transistors with the same base dopings as all HBT's, but this would not give an absolute number for the bandgap reduction due to heavy doping. Furthermore, because of alloy scattering, one might expect a different temperature dependence of D_n in Si and SiGe of similar dopings. Finally, while the $\Delta E_{G,eff}$ extracted by this method will by definition accurately model the temperature dependence of the collector current, it may not be a good predictor of the absolute value of room temperature collector current, which is more important than its temperature scaling for most modeling applications.

Therefore in this study we have chosen to make measurements of G_B and to make reasonable assumptions for D_n and the densities of states ratio, so that an absolute value of $\Delta E_{G,eff}$ (compared to undoped Si as represented by n_{i0}^2) can be extracted.

Fig. 5.6 shows a typical Gummel plot of a transistor used in this study. The collector current is ideal over several orders of magnitude, and the negligible effect of the reverse collector bias indicates no parasitic barriers due to boron outdiffusion, even for very heavy dopings in the base ($10^{20}cm^{-3}$), as confirmed by SIMS. Measurements on different area devices showed negligible perimeter effects.

Since both conduction and valence bands split in strained $Si_{1-x}Ge_x$ the effective densities of states will be lower than in Si. To take the reduction of densities of states into account, we used the model of Prinz et al.[48]. This model assumes a rigid splitting of both the conduction and valence band degeneracies due to uniaxial strain. One can then calculate the densities of states reduction factor $(N_C N_V)_{SiGe}/(N_C N_V)_{Si}$ as a function of Ge concentration and temperature. For the Ge concentrations of interest (7-27%) the reduction factor is in the range of 0.6-0.3 at room temperature. A more rigorous calculation using the band structure of [102] would give even lower value of N_V in strained $Si_{1-x}Ge_x$ (~ 0.3 for x=0.2) [94].

To model the minority carrier mobility in the base, we used the Si model of

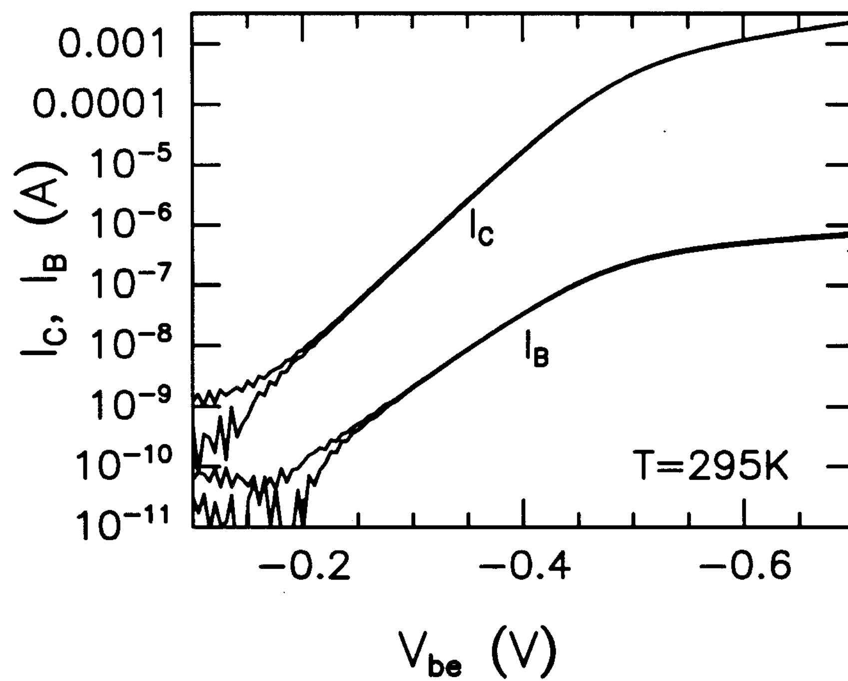

Figure 5.6: Typical Gummel plot of an HBT used in this study. Ge concentration in this device was 23% with the base doping of 3×10^{18} cm^{-3}

Swirhun et al.[85] for electron mobilities as a function of B-doping. This is a reasonable approximation since calculations by Kay and Tang [103] of minority electron mobility in strained $Si_{1-x}Ge_x$ alloys predict at most an enhancement of 20% over Si values in the doping range of interest. Note also that we observed no clear evidence of significant enhancement of lateral hole drift mobilities with increased Ge concentrations, especially at high doping levels. The base Gummel number G_B was measured directly by SIMS on the same wafer on which the devices were made. The Gummel number was also obtained by the lateral base transport measurements. The agreement with that found by SIMS was obtained within the uncertainty of 30% due to the uncertainty in the Hall scattering factor. On devices where no SIMS data was available, the Gummel number obtained by Hall measurements was used, corrected by the Hall scattering factor of Fig. 5.4. Finally, for $n^2_{io,Si}$ the accepted value of 1×10^{20} cm^{-3} at 295K was used. The estimated total uncertainty on the prefactor in equation (3) (combined uncertainty of D_n, G_B, and the densities of states ratio) was a factor of 2. This corresponds to an uncertainty of 17 meV in the extracted $\Delta E_{G,eff}$. The summary of the samples and the most relevant measured parameters is given in Table 5.1.

Using this method, Fig. 5.7 shows the extracted effective bandgap narrowing at room temperature as a function of Ge concentration for different doping levels. For the devices with similar dopings, the linear dependence on Ge concentration is obvious. Fitting the data at the same doping level gives a bandgap offset with respect to Si of $\sim$ 7meV/1%Ge. Assuming that this linear dependence on Ge concentration is independent of doping, we have separated the two effects contributing to bandgap reduction with respect to undoped Si: bandgap reduction due to Ge ($\Delta E_{G,Ge}$) and bandgap narrowing due to heavy doping effects ($\Delta E_{G,dop}$).

$$\Delta E_{G,eff} = \Delta E_{G,Ge} + \Delta E_{G,dop} \tag{5.5}$$

Assuming a $\Delta E_{G,dop}$ of the form:

$$\Delta E_{G,dop} = A + B \times \log(\frac{N_A}{10^{18}cm^{-3}}) \qquad (5.6)$$

and a linear dependence of $\Delta E_{G,Ge}$ on x as Cx, a three-parameter best fit to our data was found to be:

$$\Delta E_{G,eff} = 28.6 + 27.4 \times \log(\frac{N_A}{10^{18}cm^{-3}}) + 688 \times x \quad (meV) \qquad (5.7)$$

where N_A is the base doping and x the Ge concentration. The first two terms represent bandgap narrowing due to doping and the last term is the Ge contribution. $\Delta E_{G,eff}$ is not the measure of the actual bandgap reduction, but the *effective* (apparent) bandgap reduction, relevant for minority carrier concentration and thus electron transport across the $Si_{1-x}Ge_x$ base. The apparent bandgap is larger than the true bandgap due to valence band filling in the degenerately doped semiconductor and hence, the effects of Fermi-Dirac statistics [104]. The effective bandgap reduction is a useful parameter to model the collector current of $Si/Si_{1-x}Ge_x$ /Si HBT's and predict the enhancement over Si-base devices.

Experimental values for $\Delta E_{G,dop}$ for $Si_{1-x}Ge_x$ are obtained by subtracting the germanium contribution (688x meV) from the measured $\Delta E_{G,eff}$. These values are plotted in Fig. 5.8 vs. base doping. This is the first time that such data has been collected for such a wide range of dopings and Ge concentrations in $Si/Si_{1-x}Ge_x/Si$ HBT's. Also plotted are previously reported results by Swirhun et al.[85] and model by Klaassen et al.[89] for apparent bandgap narrowing in p-type Si. The apparent bandgap narrowing clearly increases with increased doping, as expected. No clear Ge dependence is observed after the linear dependence has been subtracted. The bandgap narrowing of 27meV/decade agrees well with the 25-33meV narrowing at various Ge concentrations with the doping increase from $5 \times 10^{17}cm^{-3}$ to $5 \times 10^{18}cm^{-3}$, obtained from temperature dependent measurements by Poortmans et al.[98].

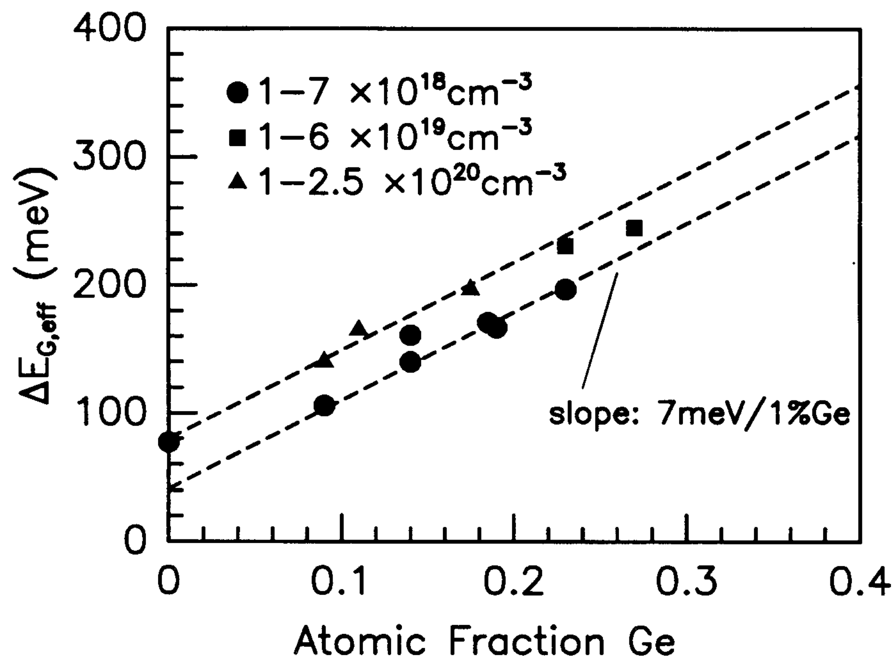

Figure 5.7: Effective bandgap reduction with respect to intrinsic Si vs. Ge concentration

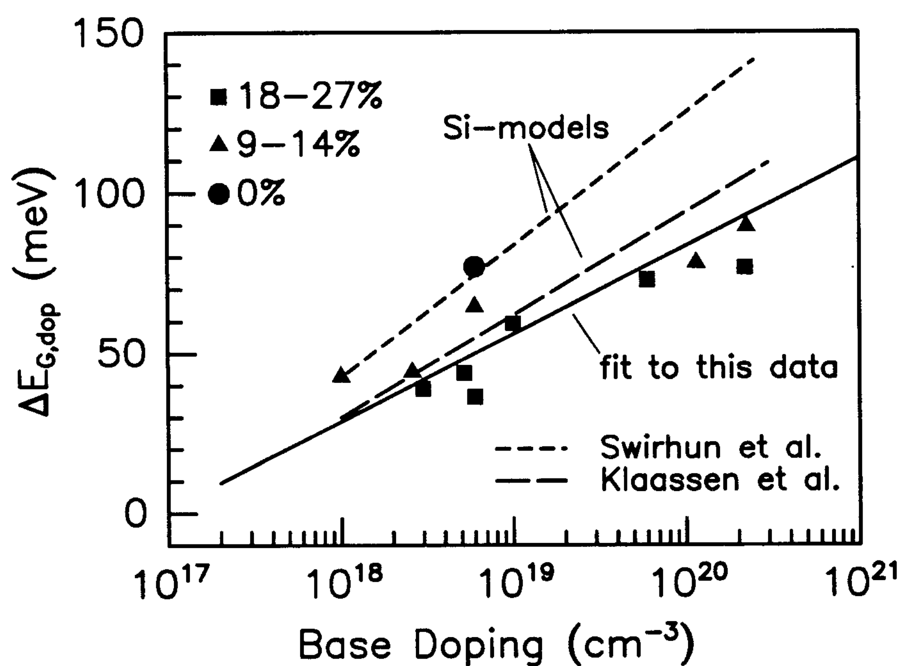

Figure 5.8: Apparent bandgap narrowing vs. base doping after linear dependence of the bandgap reduction on Ge content has been subtracted

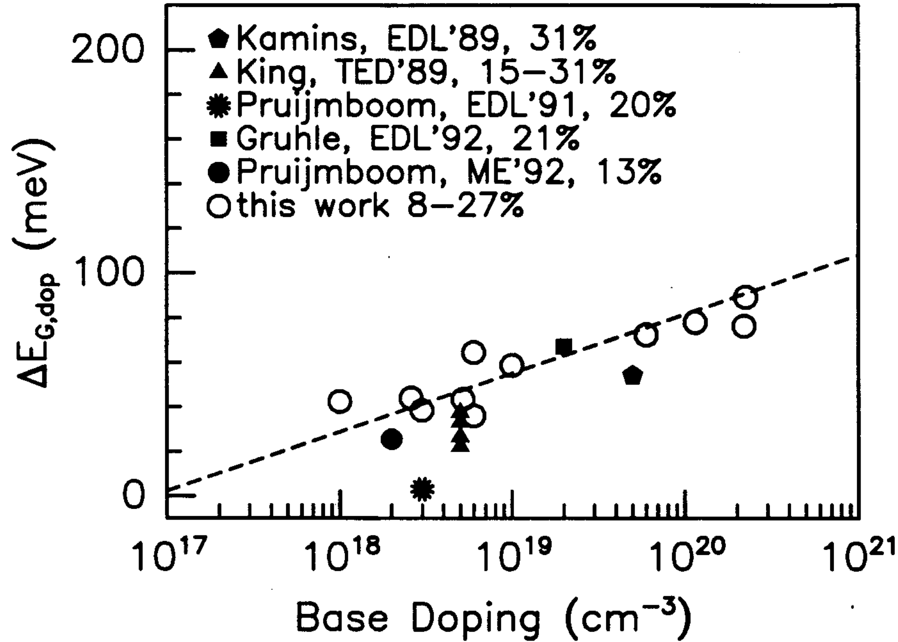

Figure 5.9: Apparent bandgap narrowing vs. base doping after linear dependence of the bandgap reduction on Ge content has been subtracted compared with data from literature

Plotted in Fig. 5.9 are data points for $\Delta E_{G,dop}$ for other SiGe HBT's reported in the literature [19, 14, 18, 24, 90], along with our data of Fig. 5.8 and the model for $\Delta E_{G,dop}$. $\Delta E_{G,eff}$, as defined in this work, was not directly given in these papers, but adequate information on base doping, base-width, collector current, etc. was given so that $\Delta E_{G,eff}$ could be calculated. $\Delta E_{G,dop}$ was then found after subtracting the linear dependence on Ge, as described earlier. In general the data of the other work also lie near our best fit for $\Delta E_{G,eff}$. It is interesting to note that nearly all of the data points which fall substantially below the best fit line are from devices which were fabricated using an implanted emitter process, which is known to give rise to excess base dopant diffusion (and possible parasitic barrier formation resulting in smaller $\Delta E_{G,eff}$) [90].

Note that our results for $\Delta E_{G,dop}$ are consistently lower than those found in Si (as

represented by the work of Swirhun [85] and Klaassen [89]), although calculations by Jain et al.[105] predict $\Delta E_{G,dop}$ to be slightly higher in SiGe than in Si, and strain-dependent. A possible explanation for smaller apparent bandgap narrowing compared to Si lies in the fact that at the same doping level, due to the band splitting and thus, reduced densities of states, the Fermi level in degenerately doped $Si_{1-x}Ge_x$ lies higher in the valence bands, and thus contributes more to the apparent bandgap reduction. To relate the apparent bandgap narrowing to the true bandgap reduction ($\Delta E_{G,true}$) one needs to know the position of the Fermi level in the degenerately doped material and take into account the effect of degenerate statistics (Fermi-Dirac instead of Boltzmann), as illustrated in Fig. 5.10. The hole concentration (doping) is related to the Fermi level (E_F) by [86]:

$$p = N_A = N_V \frac{2}{\sqrt{\pi}} F_{1/2}\left(\frac{E_V - E_F}{k_B T}\right) \tag{5.8}$$

where $F_{1/2}(E_F/k_BT)$ is the Fermi-Dirac integral. Fig. 5.11 shows the calculated position of the Fermi level with respect to the valence band edge as a function of base doping for Si and $Si_{0.8}Ge_{0.2}$ using equation 5.8 and the model of Prinz et al. [48] for the effective valence band density of states in $Si_{1-x}Ge_x$. Note that the position of the Fermi level starts to diverge from the straight line in the case of $Si_{0.8}Ge_{0.2}$ at a lower doping level, and diverges much faster with increasing doping, thus having a bigger effect on $\Delta E_{G,eff}$ than in Si at the same doping level. Possin et al. [104] have the first modeled the apparent bandgap narrowing as the sum of the true bandgap narrowing ($\Delta E_{G,true}$) and the negative term representing the Fermi-Dirac ($\Delta E_{G,FD}$) correction given as:

$$\Delta E_{G,eff} = \Delta E_{G,true} + \Delta E_{G,FD} \tag{5.9}$$

$\Delta E_{G,FD}$ is always negative and it is given by:

$$\Delta E_{G,FD} = \ln\left[e^{\frac{E_V - E_F}{k_B T}} F_{1/2}\left(\frac{E_V - E_F}{k_B T}\right)\right] = -(E_V - E_F) + k_B T \ln\frac{N_A}{N_V} \tag{5.10}$$

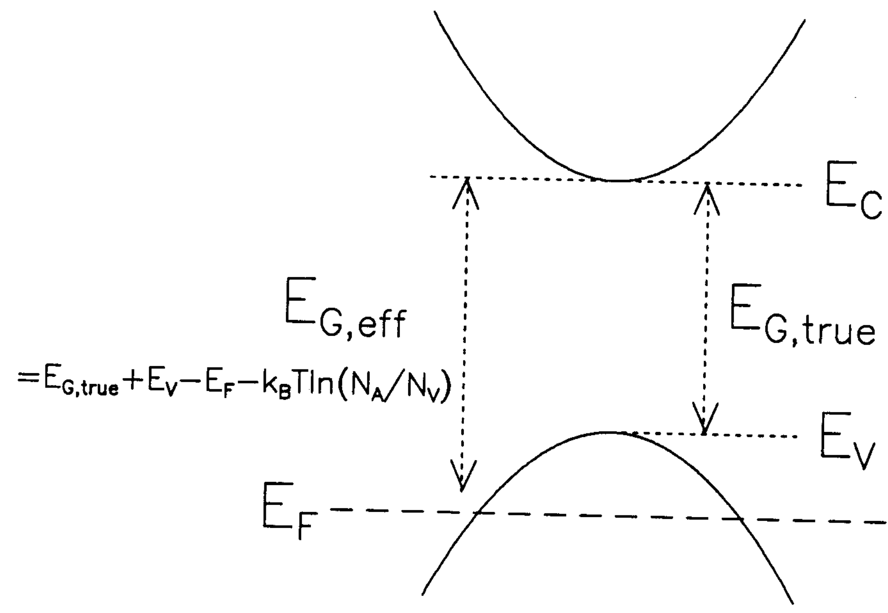

Figure 5.10: Qualitative band diagram illustrating the difference between the true and the effective bandgap

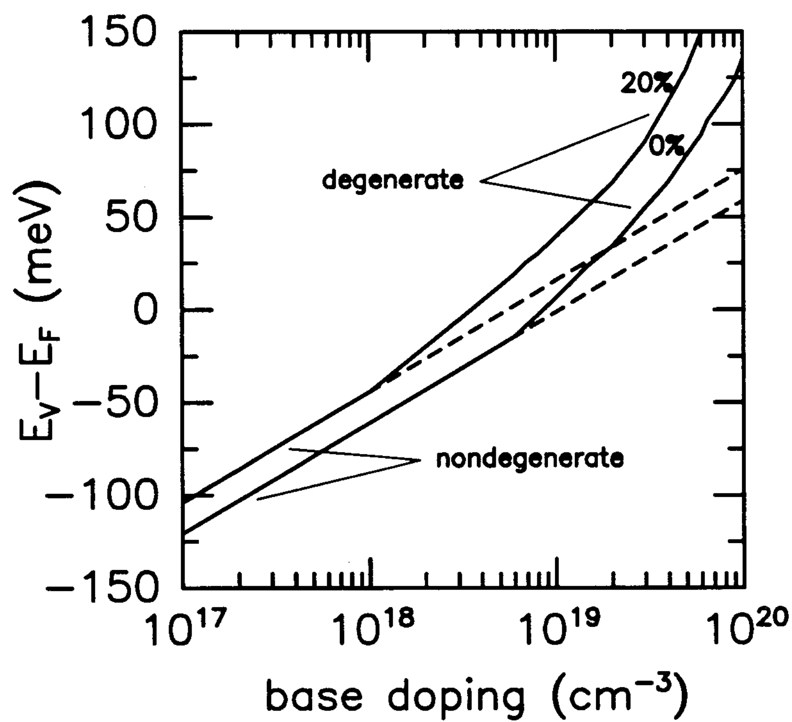

Figure 5.11: Position of the Fermi level with respect to the valence band edge for Si and $Si_{1-x}Ge_x$

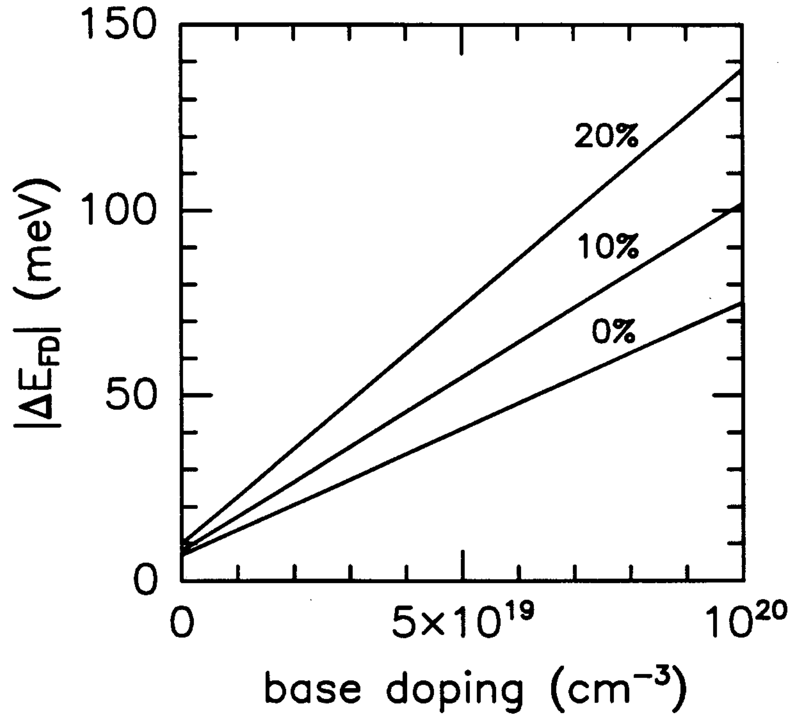

Figure 5.12: Calculated Fermi-Dirac correction to the bandgap narrowing as a function of base doping for various Ge concentrations at room temperature

Fig. 5.12 shows calculated values for $\Delta E_{G,FD}$ at room temperature as a function of doping for x = 0, 10 and 20% using equation 5.10. We have applied the $\Delta E_{G,FD}$ to our $Si_{1-x}Ge_x$ data of Fig. 5.7 and subtracted the linear Ge dependence ($\Delta E_{G,Ge} \sim$ 7meV/1%) to extract the true $Si_{1-x}Ge_x$ bandgap reduction. The results are plotted in Fig. 5.13. Also shown in the figure are the theoretical calculation for the true bandgap narrowing in p-Si by Jain and Roulston [105] (solid line) and room temperature Si-data of Wagner [106] measured by photoluminescence. The $\Delta E_{G,dop,true}$ agrees fairly well with the Si data at lower dopings, but at heavy doping levels the $Si_{1-x}Ge_x$ data lies higher. There is no clear Ge dependence on $\Delta E_{G,dop,true}$, however. If the carrier concentration effective mass of ref. [92] were used, which would result in even bigger $\Delta E_{G,FD}$, the data points would shift to even higher values of $\Delta E_{G,dop,true}$

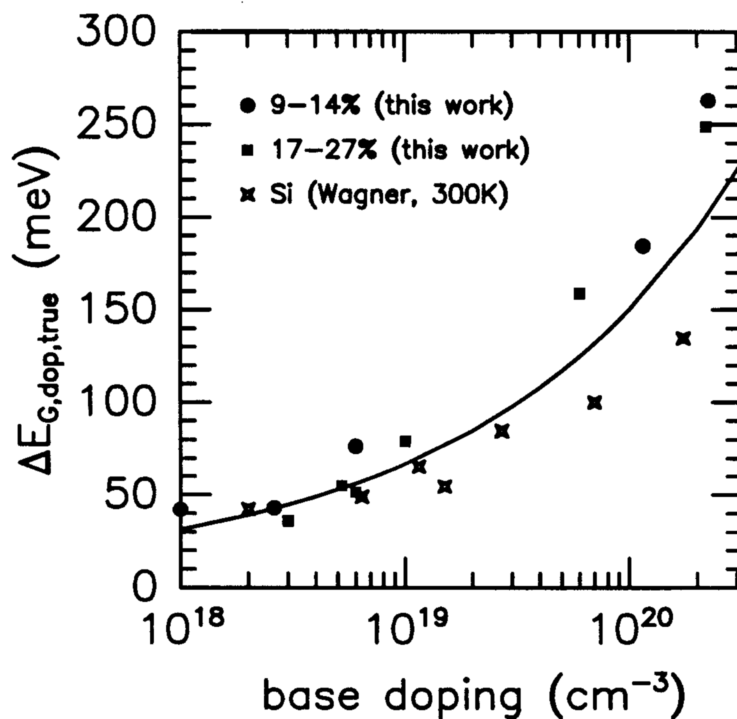

Figure 5.13: The heavy-doping contribution to the true bandgap reduction in strained $Si_{1-x}Ge_x$ calculated from the measured $\Delta E_{G,eff}$ as: $\Delta E_{G,dop,true} = \Delta E_{G,dop} - \Delta E_{G,FD}$. Also shown for comparison are the Si data points of Wagner and the theoretical calculation for p-Si of Jain and Roulston (solid line).

at high doping levels and higher Ge concentrations. On the other hand, the observed Fermi energy in p-Si is less than predicted by the conventional density of states equation (5.8) [107]. If similar behaviour were the case in $Si_{1-x}Ge_x$, this would result in overestimated $\Delta E_{G,dop,true}$. Although some uncertainty in the absolute value of $\Delta E_{G,dop,true}$ remains, the Fermi level in strained $Si_{1-x}Ge_x$ clearly lies higher than in Si for the same doping level resulting in stronger effects of degenerate statistics. Thus, the weaker doping dependence and lower values compared to Si data of the apparent $\Delta E_{G,dop}$ are attributed to the larger effect of $\Delta E_{G,FD}$ in $Si_{1-x}Ge_x$ than in Si.

5.5 Collector current vs. base resistance model

The two important parameters for the DC design of $Si_{1-x}Ge_x$ HBT's is the base sheet resistance and the collector current enhancement with respect to Si. The base sheet resistance is important for high-speed application of $Si_{1-x}Ge_x$ HBT's and is often more easier measured (and more relevant) than the actual doping in the base or the integrated hole concentration. The effective bandgap reduction determines the collector current enhancement factor over the similarly doped all-Si device. By using $R_s = (q\mu_p G_B)^{-1}$ one can rewrite equation 5.4 to model the collector current as a function of these two parameters:

$$J_{co} = q^2 \frac{(N_C N_V)_{SiGe}}{(N_C N_V)_{Si}} n_{io,Si}^2 D_n \mu_p R_{B,sheet} e^{\frac{\Delta E_{G,eff}}{k_B T}} \tag{5.11}$$

where μ_p and D_n are the lateral drift hole mobility and vertical electron diffusion coefficient in p^+-base, respectively. Equation 5.11 shows a clear trade-off between collector current (gain) and base sheet resistance. This is summarized in Fig. 5.14. The relative collector current with respect to Si is plotted as a function of base sheet resistance for various Ge concentrations. A relative collector current factor of one is defined for Si at a base sheet resistance of 1kΩ/sq. The lines are the model calculations

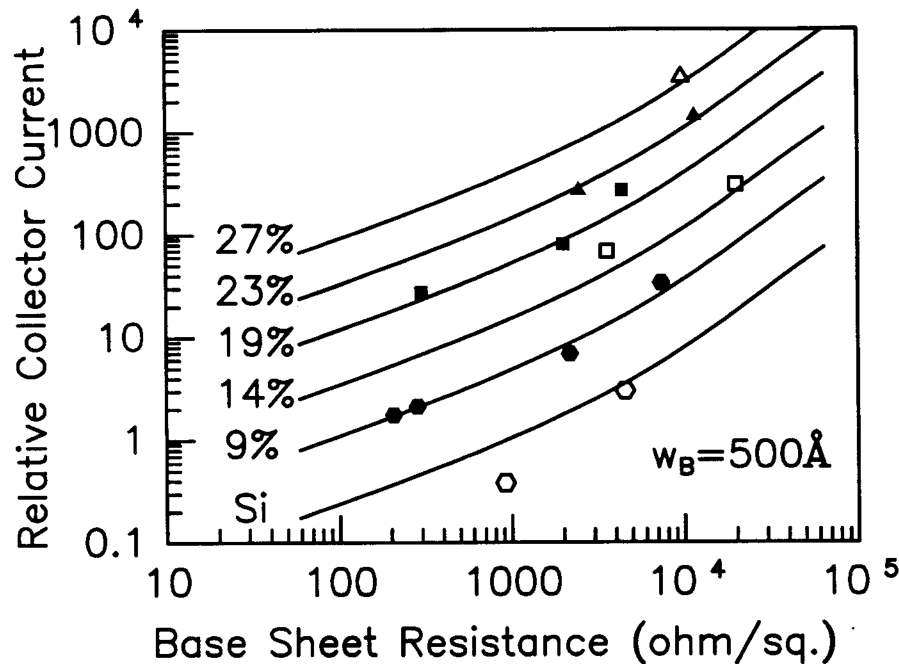

Figure 5.14: Relative collector current vs. base sheet resistance. The lines correspond to the model, the points are the data

assuming base widths of 500Å, hole drift mobilities given by equation 5.1, bandgap reduction by equation 5.7, strain-induced correction for densities of states given by [48] and electron mobility by [85]. The points are measured data in our HBT's scaled to 500Å base-widths. Note especially the effect of the bandgap narrowing due to heavy base doping which has a more significant effect than the lateral and vertical mobility reduction at heavy dopings. The bandgap narrowing causes curves not to be linear, and limits the reduction in collector current at low base resistances.

5.6 Summary

This chapter provides a comprehensive study of majority carrier properties in heavily B-doped strained $Si_{1-x}Ge_x$ layers as well as collector currents of HBT's in the

sample number	Ge (%)	G_B -SIMS ($10^{14}cm^{-2}$)	G_B -Hall ($10^{14}cm^{-2}$)	N_A ($10^{19}cm^{-3}$)	doped w_B (Å)	$R_{B,sheet}$ (kΩ/sq.)	J_{co} (nA/cm²)	$\Delta E_{G,eff}$ (meV)
933	0	4.2	3.8	4.3	980	0.475		
934	11	14.7	13.4	22.5	660	0.16	0.020	165
935	18.5	0.17	0.27	0.52	400	6.29	2.203	171
936	17.5	4.78	6.2	22.0	400	0.36	0.1712	197
937	23		0.03	0.31	160	36.25	84.31	197
938	23		1.4	5.9	160	7.5	4.878	231
939	23		2.6	12.0	80	0.88		
940	27		0.44	1.0	175	27.89	32.06	245
946	27		4.8	13.0	90	0.98		
947	9	0.47	0.52	0.26	1830	2.26	0.0871	106
948	9		15.0	8.3	1800	0.16		
949	9	14.2	16.0	11.5	1190	0.12	0.0086	140
633	0		0.27	0.45	600	3.8	0.0869	77
636	14		0.43	0.61	650	3.2	0.7505	161
641	24		0.21	0.23	400	5.8		
642	14		0.062	0.1	600	18.0	4.109	140
643	21		0.69	0.6	600	2.0	1.537	186

Table 5.1: Summary of HBT samples and relevant parameters (G_B -SIMS is the raw data uncorrected for depletion region effects, G_B -Hall is calculated assuming $r_H = 1$)

wide range of dopings and Ge concentrations for the first time [108]. The hole Hall mobility decreases with increasing Ge concentration at a fixed doping level, because the Hall scattering factor decreases as Ge is added. The lateral hole drift mobility remains approximately constant as Ge is added, with perhaps a slight increase at low doping levels. The apparent bandgap narrowing in p-type strained $Si_{1-x}Ge_x$ was measured for the first time over a wide range of doping and Ge levels. The dependence of the narrowing on Ge was independent of doping, and the heavy doping contribution to the effective bandgap narrowing is found to be independent of Ge concentration but slightly lower than that obtained for Si at the same doping level,

attributed to the Fermi-Dirac statistics effect. Finally, a trade-off between the collector current enhancement and base sheet resistance is presented for DC modeling of $Si_{1-x}Ge_x$ HBT's. The bandgap narrowing at heavy doping levels (low base sheet resistances) has a larger impact than that of reduced mobility at high doping levels.

Chapter 6

Minority Carrier Properties in $Si_{1-x}Ge_x$

6.1 Introduction

Bipolar transistors rely on minority carrier transport across the device. This is why accurate modeling of minority carrier transport deserves a lot of attention. Important parameters to characterize it are minority carrier mobility (μ_n in p-type material), minority carrier lifetime (τ_n), and minority carrier diffusion length (L_n), which are related by:

$$L_n = \sqrt{D_n \tau_n} \tag{6.1}$$

where D_n is the diffusion coefficient ($D_n = \mu_n \times k_B T/q$). The collector current density of a bipolar transistor in forward active mode is given by:

$$J_C = \frac{q D_n n_i^2}{N_A L_n \sinh(w_B/L_n)} e^{\frac{qV_{BE}}{k_B T}} \tag{6.2}$$

In case of narrow bases ($w_B << L_n$) equation 6.2 simplifies to 5.3 for DC collector current. In the previous chapter, we have measured n_i^2 (i.e. E_G) in doped $Si_{1-x}Ge_x$ assuming that D_n is the same as in silicon (given by [84]). Although this assumption might be reasonable considering no significant Ge-dependence on majority hole mobility in heavily doped HBT bases, the accurate values of minority carrier mobility still need to be determined in strained $Si_{1-x}Ge_x$ alloys.

It has been experimentally observed that the minority carrier mobility in heavily doped silicon is larger than majority carrier mobility [85, 84]. The difference between majority and minority mobilities are not surprising, since apart from heavy doping effects on the bandgap structure, the dominant impurities for electron scattering become acceptors instead of donors, i.e. majority carriers are holes instead of electrons. Both electron-hole and electron-electron scattering need to be taken into account. The temperature dependence of minority carrier mobility is also very different from the majority [101]. In case of strained $Si_{1-x}Ge_x$ alloys, the minority carrier mobility is also expected to be affected by strain and alloy scattering.

One could independently determine the minority carrier diffusion coefficient in strained $Si_{1-x}Ge_x$ by measuring both the lifetime and minority carrier diffusion length. In this chapter, we report the design of the lateral device structure for diffusion length and lifetime measurements and diffusion length results for strained $Si_{1-x}Ge_x$ layers in the p-type doping range of 2×10^{17} cm^{-3} to 4×10^{18} cm^{-3}.

6.2 Methods to measure minority carrier diffusion length and mobility

In silicon, many types of device structures have been used over the years by various authors to extract minority carrier properties. A critical review of measurements previously reported is included in the work of del Alamo [96] and Swirhun [97].

Since collector current in a bipolar transistor is a clean monitor of minority carriers through the base and it is ideal with respect to base-emitter voltage, del Alamo [96] and Swirhun [97] have reported a comprehensive set of diffusion length measurements on lateral bipolar transistors for n and p-type Si, respectively (the method first used by Wieder [109]). In case of wide-base bipolar transistor ($w_B >> L_n$) from equation

6.2 collector current becomes:

$$I_C = A\frac{2qD_n{n_i}^2}{N_A L_n}\, e^{\frac{-w_B}{L_n}}\, e^{\frac{qV_{BE}}{k_B T}} \tag{6.3}$$

In case of lateral devices A is the collecting area which includes two-dimensional effects. The lateral devices were obtained by implantation of emitter and collector into the base material. From the collector current measurements on devices with various basewidths, the diffusion length was determined by fitting I_C vs. w_B.

Minority carrier mobility cannot be extracted just from DC measurements. To measure minority carrier mobility a time-dependent technique needs to be used. For example, if one independently measured lifetime, the mobility could be extracted by combining the lifetime with the diffusion length measurements. The lifetime at heavy doping levels is expected to be a fundamental property of the material due to recombination dominated by Auger processes. No data on minority carrier lifetime is available for $Si_{1-x}Ge_x$ at present.

Lifetime can be measured by decay of photoluminescence radiation of electron-hole pairs after excitation by a short laser pulse [110, 111, 85]. Since band-edge photoluminescence has been observed in $Si_{1-x}Ge_x$ alloys [65] one could essentially measure lifetime. However, photoluminescence from $Si_{1-x}Ge_x$ quantum wells has only been observed at low temperatures which restricts lifetime measurements to below room temperature. Minority carrier lifetime could also be measured as a decay of photoexcited carriers, as proposed by Stevenson and Keyes [112]. The excess carrier generated by light pulses cause a momentary increase in the conductivity. The decay of that conductivity is a measure of lifetime. Another method to measure lifetime is from AC diffusion length measurements, as demonstrated by Dziewior and Silber [113], since the diffusion length measured at frequency ω is related to the DC (L_0) value by:

$$L(\omega) = \frac{L_0}{\sqrt{1 + j\omega\tau}} \tag{6.4}$$

Misiakos et al. [114] have proposed a method for simultaneous measurement od diffusion coefficient, lifetime and diffusion length based on lateral collection of photogenerated carriers by a semi-infinite junction by DC measurements and transient response in the frequency domain.

To our knowledge, the only reported measurement of the electron diffusion coefficient in $Si_{1-x}Ge_x$ by King et. al. [14] was based on DC measurements on vertical HBT collector current. He was forced to make the assumption of no differences in densities of states between Si and strained $Si_{1-x}Ge_x$ and that minority carrier diffusion coefficients in Si and $Si_{1-x}Ge_x$ have the same temperature dependence. Furthermore, high values of oxygen contamination (1×10^{20} cm^{-3}) were present in these $Si_{1-x}Ge_x$ layers.

We have designed a lateral device structure for the diffusion length measurements. Although one cannot provide a bulk strained $Si_{1-x}Ge_x$ material, one can optimize layer structure such that the lateral minority carrier current transport is dominated by the transport through a thin $Si_{1-x}Ge_x$ layer. This is possible due to conduction band offset between p^+-Si and p^+-$Si_{1-x}Ge_x$. However, special care needs to be taken to prevent parallel Si transport, as well as loss of carriers due to surface recombination. The same structure could be used for lifetime measurements by monitoring the decay of photoconductivity [112] or, at low temperatures, by measuring photoluminescence decay. The following sections discuss the proposed device structure and the design details, as well as initial diffusion length measurements.

6.3 Structure optimization for measurements of minority carrier parameters in strained SiGe alloys

Due to strain relaxation constrains (see chapter 2) $Si_{1-x}Ge_x$ material can only be fabricated in thin layers, on the order of 100–1000Å. That makes it impossible to

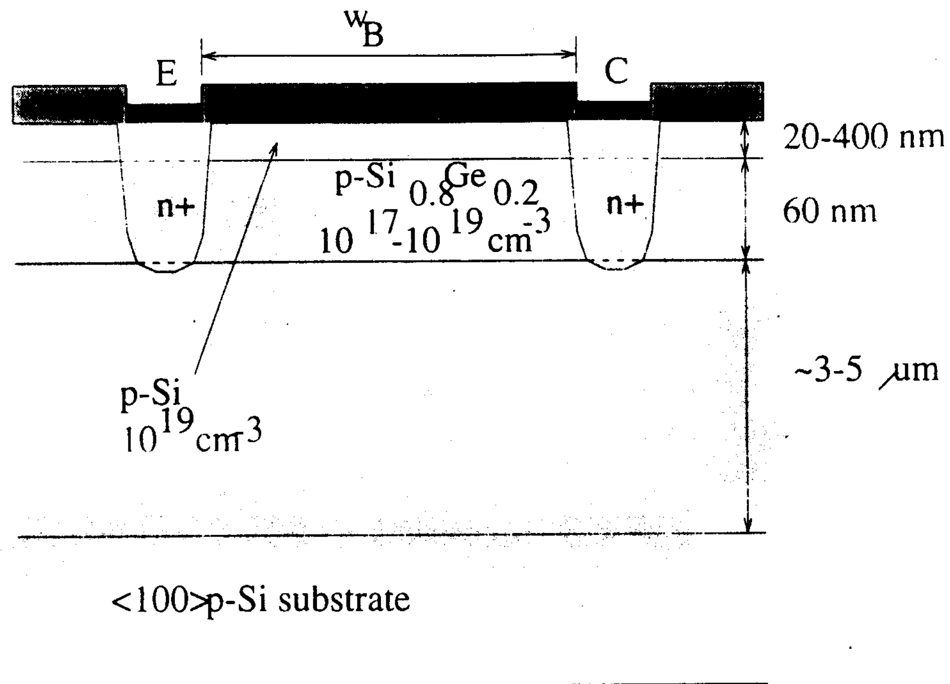

Figure 6.1: Device structure optimized using MEDICI (2D simulator) for diffusion length measurements

design vertical "long-base" devices, so "long-base" device structures are limited to lateral transport. An issue that needs to be solved in lateral devices is the confinment of minority carriers within the thin $Si_{1-x}Ge_x$ layer. However, in case of p-Si/p-$Si_{1-x}Ge_x$/p-Si heterostructures, since the bandgap of strained $Si_{1-x}Ge_x$ is smaller than silicon bandgap, it is reasonable to assume that most of electrons are going to be confined within the $Si_{1-x}Ge_x$ layer. Such heterostructures were optimized using 2D device simulation program (MEDICI) by simulating lateral bipolar transistors for diffusion length measurements. The structure is shown in Fig. 6.1. The emitter and collector would be fabricated by ion implantation and annealing. The distance between the emitter and collector implant determines the basewidth w_B. Fig. 6.2

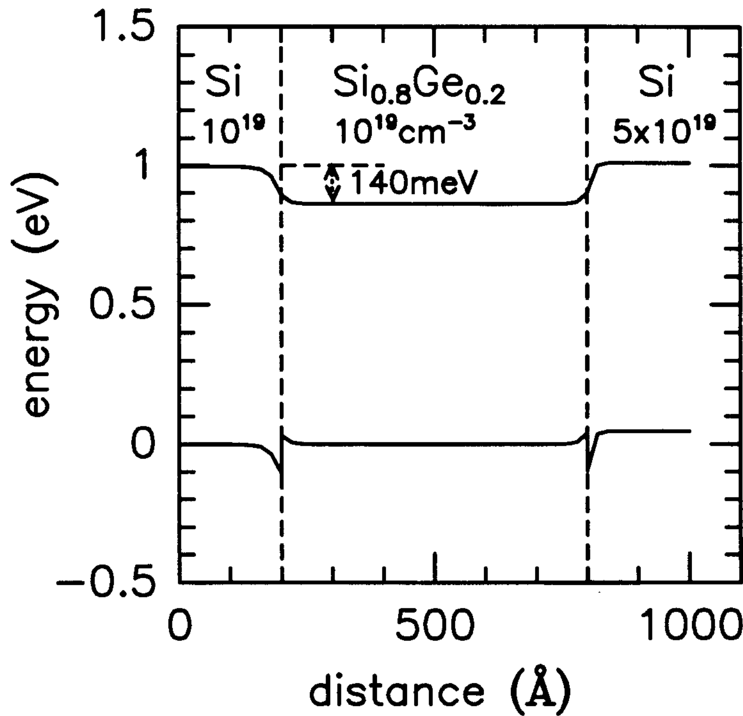

Figure 6.2: Simulated band diagram of p^+-Si/p^+-$Si_{0.8}Ge_{0.2}$/p^+-Si

shows the simulated band diagram of a p^+-Si/p^+-$Si_{0.8}Ge_{0.2}$/p^+-Si heterostructure. For $\sim$ 20% germanium in the $Si_{1-x}Ge_x$ layer the conduction band difference is $\sim$ 140meV between the Si and $Si_{1-x}Ge_x$.

In lateral bipolar transistors, the collector current is inversely proportional to $\exp(w_B/L_n)$ (equation 6.3), so the slope of the measured collector current, on a logarithmic scale, vs. w_B gives the diffusion length. To first order the ratio of lateral currents in $Si_{1-x}Ge_x$ and Si is given by:

$$\frac{I_C(SiGe)}{I_C(Si)} \approx \frac{A(SiGe)}{A(Si)} \frac{N_A(Si)}{N_A(SiGe)} \frac{N_C N_V(SiGe)}{N_C N_V(Si)} e^{\frac{\Delta E_G}{k_B T}} \tag{6.5}$$

The thicker the $Si_{1-x}Ge_x$ layer, more current will flow through $Si_{1-x}Ge_x$. The thickness of the $Si_{1-x}Ge_x$ layer is limited by the critical thickness. The implants need to be shallow to minimize the collecting area in silicon. The higher the doping in

surrounding Si layers the better is the current ratio (i.e. less current in Si), until the doping level is reached to start causing significant bandgap narrowing or leakage currents in p^+–n^+ junctions. The losses of minority carriers to the substrate or to the surface also need to be taken into account. The doping and the thickness of the bottom Si layer were optimized for negligible substrate effects. For p-type Si doped 1×10^{19} cm^{-3} the required thickness was found to be at least 3μm. The models of Swirhun [97] for minority carrier parameters were used in the simulation.

Fig. 6.3 shows collector currents vs. base-emitter voltage for the above structure (N_A(SiGe) = 1×10^{19} cm^{-3}, N_A(Si) = 5×10^{19} cm^{-3}), as well as bulk Si (N_A = 1×10^{19} cm^{-3}, no $Si_{1-x}Ge_x$ channel), and bulk $Si_{1-x}Ge_x$ (possible in simulation, $N_A = 1 \times 10^{19}$ cm^{-3}) devices when no surface recombination is present and $w_B \approx 4L_n$. The collector current in $Si_{0.8}Ge_{0.2}$ channel device (realistic structure) is almost identical to the bulk $Si_{0.8}Ge_{0.2}$ device. However, the collector current in the all-Si device is much lower ($\sim \exp(-\Delta E_G/k_BT)$). The simulations confirmed the exponential dependence of the collector current on basewidth and that the extracted diffusion lengths were the same in case of bulk $Si_{0.8}Ge_{0.2}$ and $Si_{0.8}Ge_{0.2}$-channel devices. To further confirm that the lateral electron transport is mainly through the $Si_{0.8}Ge_{0.2}$ layer, simulations with different mobilities in Si and $Si_{0.8}Ge_{0.2}$ were performed. This is shown in Fig. 6.4. The increase in electron mobility in the $Si_{0.8}Ge_{0.2}$ layer increases the collector current, while the change in electron mobility in Si does not affect the current.

After the preliminary structure was designed, surface recombination was introduced in the simulations. Significant surface recombination could cause the measured diffusion length to appear lower than the true one due to a lower effective lifetime. If the effective lifetime were measured independently, one could still extract the correct minority carrier diffusion coefficient in the $Si_{1-x}Ge_x$ layer, but not the true lifetime. To first order, if the cap Si layer is thin ($<< L_n$) and the surface recombination veloc-

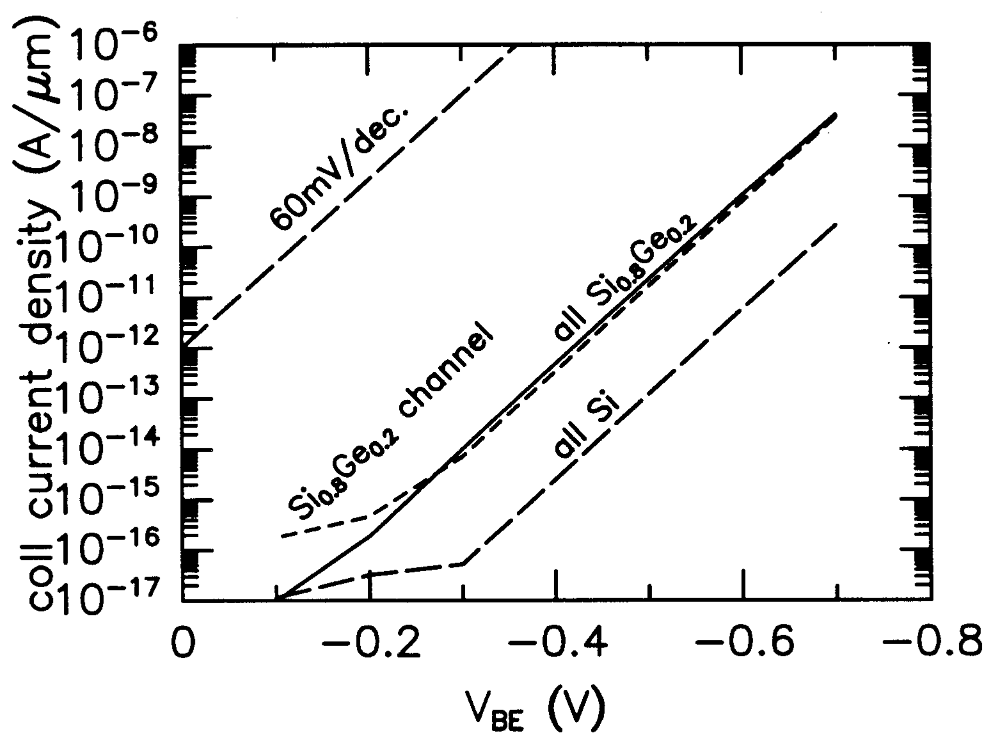

Figure 6.3: Simulated collector current density for a $Si_{0.8}Ge_{0.2}$ channel device (w_{SiGe} = 600Å, $N_A(SiGe) = 1 \times 10^{19}$ cm^{-3}, $N_A(Si) = 5 \times 10^{19}$ cm^{-3}, $w_{Si,cap}$ = 200Å, $w_{Si,buffer} = 5\mu m$, $w_B = 15\mu m$), and bulk Si and bulk $Si_{0.8}Ge_{0.2}$ devices, ($N_A = 1 \times 10^{19}$ cm^{-3}, $w_{vertical} = 20\mu m$, $w_B = 15\mu m$ in both cases)

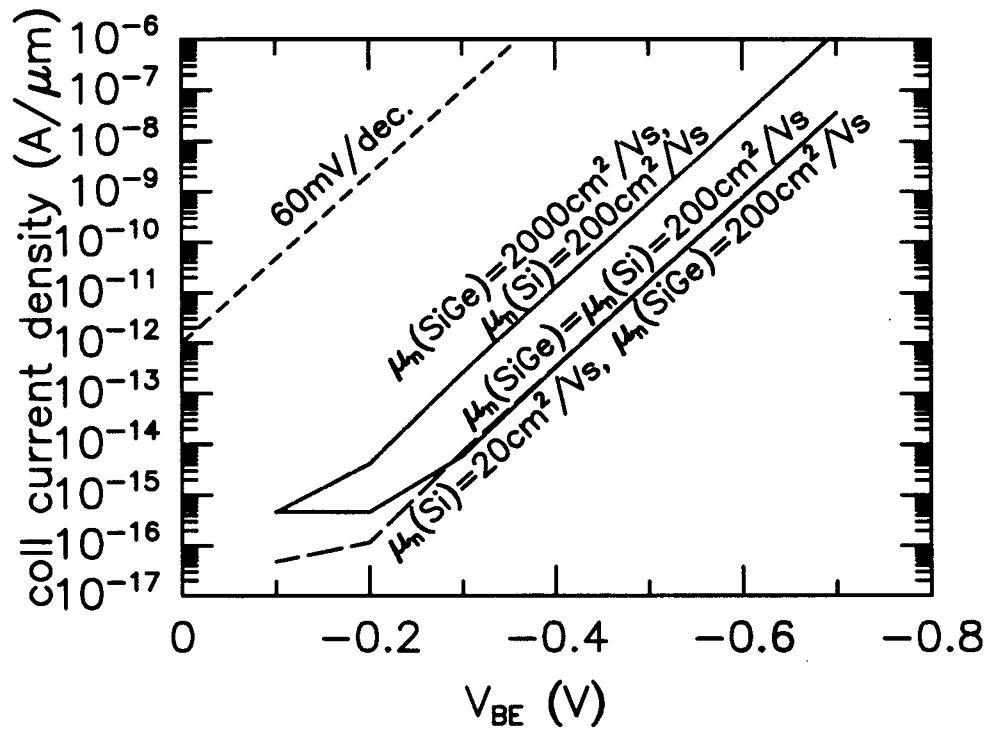

Figure 6.4: Simulated collector current density for a $Si_{0.8}Ge_{0.2}$ channel device ($w_{Si,cap}$ = 200Å, w_{SiGe} = 600Å, $w_{Si,buffer}$ = 5μm) when electron mobilities in Si and $Si_{0.8}Ge_{0.2}$ layers are varied

ity slow compared to $D_{n,Si}/w_{Si,cap}$ so that the electron quasi Fermi level at the surface is the same as that in the $Si_{1-x}Ge_x$, one can write:

$$(\frac{dn}{dt})_{SiGe} = \frac{n_{SiGe}}{\tau_{n,eff}} = \frac{n_{SiGe}}{\tau_{n,SiGe}} + \frac{n_{SiGe}}{w_{SiGe}} S_{eff}\, e^{\frac{-\Delta E_G}{k_B T}} \tag{6.6}$$

where n_{SiGe} is the electron concentration in $Si_{1-x}Ge_x$, $\tau_{n,eff}$ is the measured lifetime, $\tau_{n,SiGe}$ is the true lifetime in $Si_{1-x}Ge_x$, S_{eff} is the surface recombination velocity (accounting for any band banding effects at the Si surface) and w_{SiGe} is the thickness of the $Si_{0.8}Ge_{0.2}$ layer. The effective lifetime can be modeled as:

$$\tau_{n,eff} = \left(\frac{1}{\tau_{n,SiGe}} + \frac{S_{eff}}{w_{SiGe}} e^{\frac{-\Delta E_G}{k_B T}}\right)^{-1} \tag{6.7}$$

This is illustrated in Fig. 6.5 where the effective lifetime is plotted as a function of the true lifetime for different S_{eff}. The τ_n range in the figure approximately corresponds to the 1×10^{18} cm^{-3} to 5×10^{19} cm^{-3} p-type doping range in Si [97]. For surface recombination to have negligible effects, the following needs to hold:

$$S_{eff} e^{\frac{-\Delta E_G}{k_B T}} << \frac{w_{SiGe}}{\tau_{n,SiGe}} \tag{6.8}$$

Assuming the same minority carrier lifetimes in $Si_{1-x}Ge_x$ as in Si ($\sim$ 10ns), S_{eff} should be below $\sim 10^4$cm/s. The simulation gives an upper limit to S_{eff} of 6000cm/s. By increasing the thickness of the top Si layer the surface effects are reduced, but thinner top layers are desired for high lateral current ratio (equation 6.5). The thickness for $S_{eff} \sim 10^5$cm/s needs to be above 5000Å.

6.4 Device fabrication

A set of structures was grown to measure minority carrier parameters. A thick (3-5μm) p^+(1×10^{19} cm^{-3}–5×10^{19} cm^{-3}) Si buffer layer was grown to prevent the diffusion of carriers to p^- Si substrate in all samples. $Si_{0.8}Ge_{0.2}$ layers 600Å thick and 300Å thick were grown with the doping levels varying from 3×10^{17} cm^{-3} to

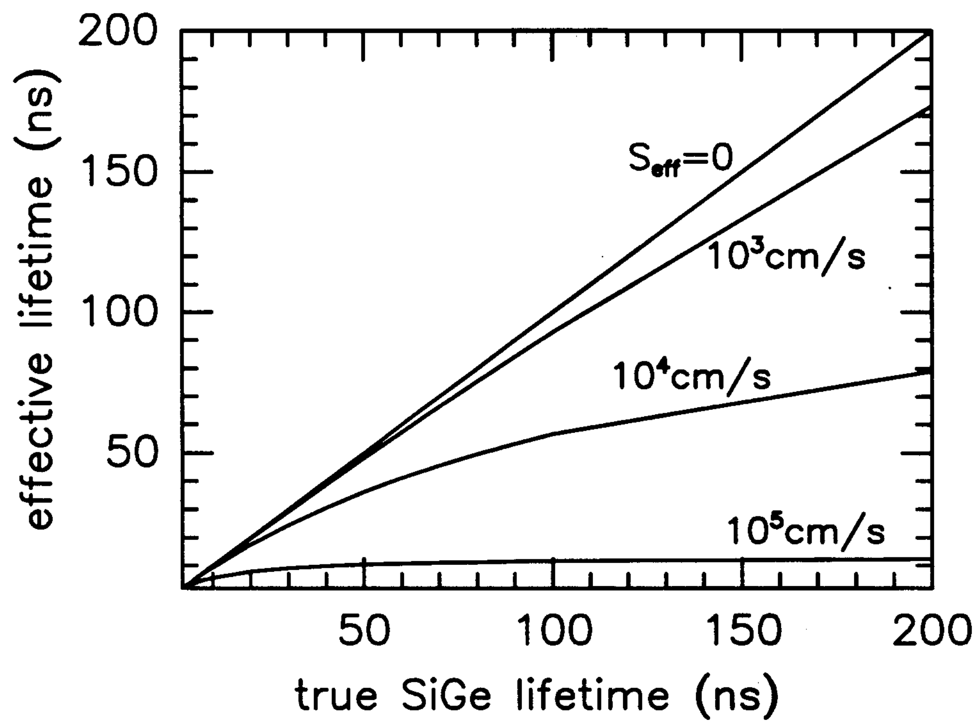

Figure 6.5: Effective lifetime as a function of true lifetime for various surface recombination velocities

sample number	B_2H_6flow (sccm) (10ppm in H_2)	$Si_{0.8}Ge_{0.2}$ thickness (Å) by SIMS	Si cap thickness (Å) by SIMS	$Si_{1-x}Ge_x$ doping ($10^{18}cm^{-3}$) by SIMS
1567	11	480	4360	3.2
1568	11	240	4480	3.8
1569	0.8	400	4320	0.26
1570	2.5	440	4120	0.7
1571	6.2	504	4000	1.7
1572	5	400	240	1.2
1573	7	400	230	2.5
1574	7	180	240	2.7

Table 6.1: Summary of structural parameters of samples designed for measurements of minority carrier properties

4×10^{18} cm^{-3}. Both structures with thick ($\sim$ 4000Å) and thin ($\sim$ 200Å) p^+Si-cap layers were grown (1.5×10^{19} cm^{-3}–2×10^{19} cm^{-3}). The layer thicknesses and doping levels were measured by SIMS. The actual doping in the $Si_{1-x}Ge_x$ layers measured by SIMS was lower (by a factor of 2-3) than expected from B_2H_6 flows in all samples. The actual $Si_{1-x}Ge_x$ layer thicknesses were also lower than predicted from the expected growth rate (by $\sim$1.5). The summary of samples and relevant structure parameters is given in Table 6.1.

To measure the electron diffusion length, we have fabricated devices similar to that of Fig. 6.1 except that the minority carriers were generated by light illumination instead of a forward biased p–n junction. This method was proposed by Misiakos et al. [114]. It is shown in Fig. 6.6.

To minimize the surface recombination, a high quality thermal oxide is desired at Si/SiO_2 interface. However, processing of $Si/Si_{1-x}Ge_x$ heterojunctions is restricted to temperatures below 800°C. We have used a thin layer ($\sim$ 50Å) of thermal oxide

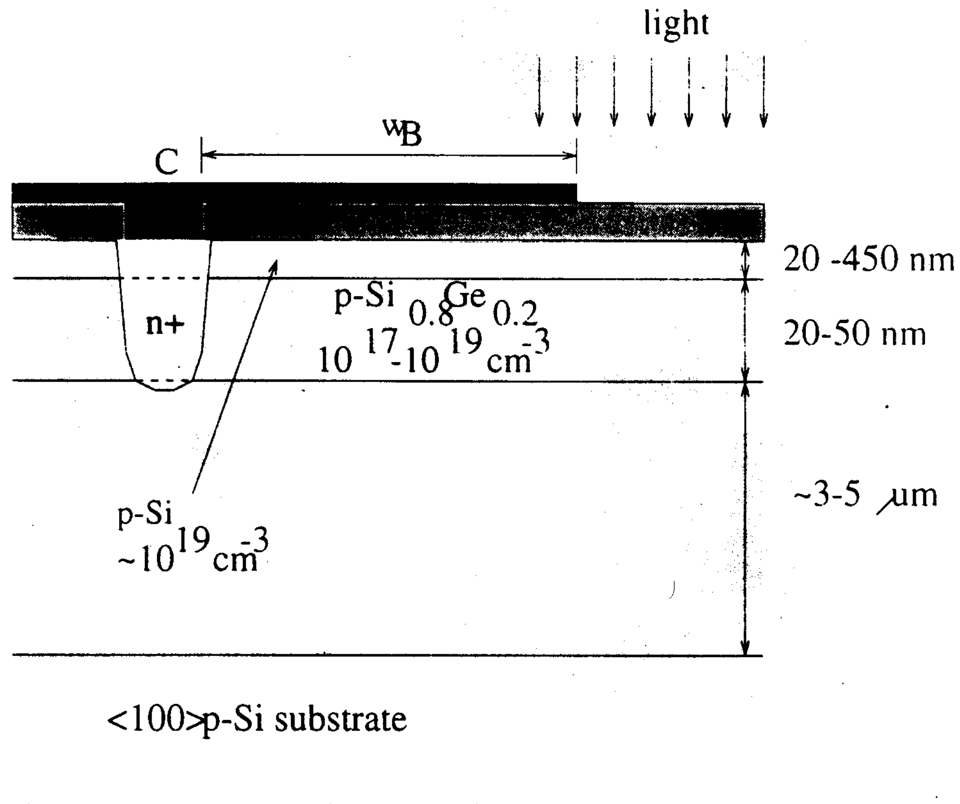

Figure 6.6: Device structure used for diffusion length measurements. The collector contact area was $150 \times 150\mu m^2$, the basewidths ranged from $1\mu m$ to $30\mu m$.

grown at 700°C (10 min. dry O_2 + 40 min wet H_2O + 5 min. dry O_2 + 10 min N_2), as an interface layer, and then deposited 5000Å thick plasma oxide at low temperature (350°C). A surface recombination velocity of below 1000cm/s is predicted for 2×10^{19} cm^{-3} p-type substrate for a dry O_2 oxidation followed by an argon anneal for a high quality Si/SiO_2 interface [115]. Assuming another factor of 10 higher S_{eff} due to possible lower quality of our thermal oxides would still give negligible effects.

The oxide was used as an ion implantation mask. Four various implant conditions (both P and As) were used to form the collector. The summary of implant conditions is given in Table 6.2. On some of the samples with thick Si caps, the Si cap layers very partially etched prior to implantation to reduce the Si current path. Device with different implants were processed simultaneously, for comparison. All the implants were annealed at 700°C for 20 minutes.

The entire p-n junction area was covered by the metal contact which laterally extended over the passivating oxide to provide a mask for the uniform light beam, as shown in Fig. 6.6. On one side of the contact the shaded area extended up to a distance w_B (varied $1 - 30\mu m$) while it was much larger on the other sides ($150\mu m$). This provides the photocurrent that is a function of basewidth w_B (see the following section).

Ti/Al metalization was used as the collector contact. Devices with 1000Å and 2000Å thick metal were fabricated.

6.5 Diffusion length measurements

Misiakos et al. [116] have derived an analytical expression for lateral photocurrent assuming a thick bulk material. In case of p-Si/p-$Si_{1-x}Ge_x$/p-Si structure, the exact expression becomes complicated, but since most of carriers generated are going to be

run	implant conditions	expected depth (SUPREM)
I 1572-1574, not etched 1569-1571 etched 4000Å	P 1×10^{15} cm^{-2},20KeV	900Å
II 1569-1571, etched 1000Å	P 1×10^{15} cm^{-2},20KeV $+ 1 \times 10^{15}$ cm^{-2},60KeV $+ 1 \times 10^{15}$ cm^{-2},100KeV $+ 1 \times 10^{15}$ cm^{-2},150KeV	3500Å
III 1569-1571, etched 2000Å	P 1×10^{15} cm^{-2},20KeV $+ 1 \times 10^{15}$ cm^{-2},60KeV $+ 1 \times 10^{15}$ cm^{-2},100KeV	2500Å
IV 1569-1571, etched 1000Å 1572-74, not etched	As 2×10^{15} cm^{-2},10KeV $+ 1 \times 10^{15}$ cm^{-2},60KeV $+ 1 \times 10^{15}$ cm^{-2},110KeV	1400Å

Table 6.2: Summary of processing runs and implant conditions

confined to $Si_{1-x}Ge_x$ layer, one can approximate photocurrent as:

$$J_{ph} \approx \int_{w_B}^{\infty} qGe^{-x/L_n}dx = qGL_n e^{-w_B/L_n} \tag{6.9}$$

where G is the generation rate of carriers per unit area. The exponential dependence on basewidth is the same as in case of a bipolar transistor ($I \propto e^{-w_B/L_n}$), as expected.

A typical measured photogenerated current vs. basewidth is plotted in Fig. 6.7. That the measurement was not affected by the absorption length of the incident light was confirmed by measurements with visible light (microscope lamp on the probe station) and 1.2μm laser. In the case of a visible light source, carriers were mostly generated in Si layers and diffused into the $Si_{1-x}Ge_x$ well, while with 1.2μm light source most of the carriers were probably generated within the $Si_{1-x}Ge_x$ layer. No

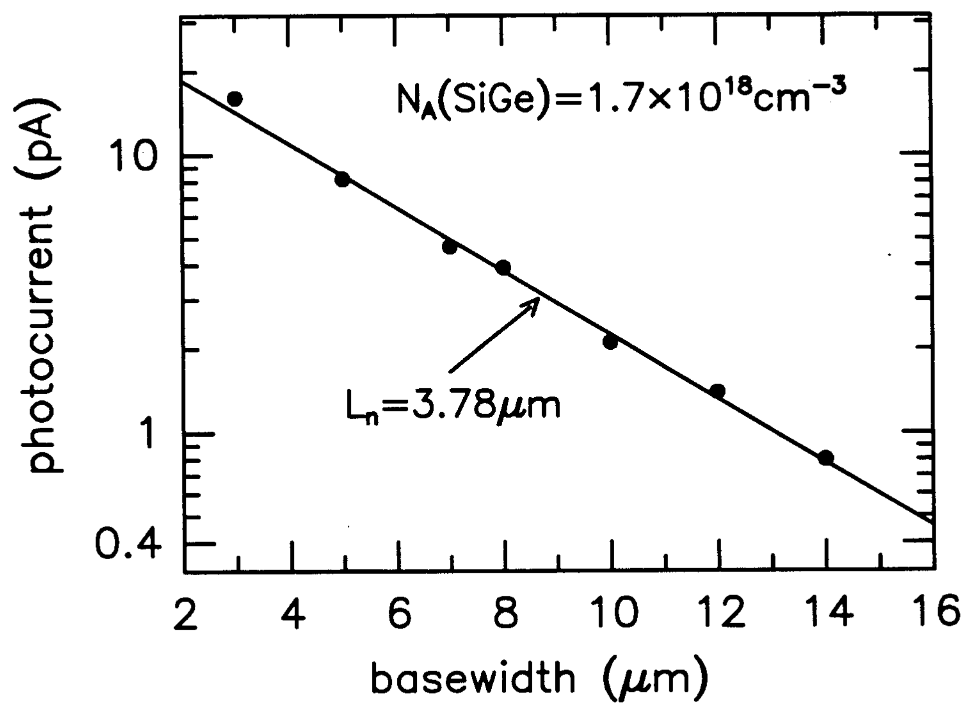

Figure 6.7: Photocurrent vs. basewidth for $N_A = 1.7 \times 10^{18}$ cm^{-3} in $Si_{0.8}Ge_{0.2}$ layer

difference in the results was observed, within the experimental error. The collector currents were measured at zero bias using HP-4140B pA-meter. The collector currents in devices with thin metal (1000Å) mask did not approach zero at very large basewidths ($\sim 10L_n$), but rather a constant background current, probably because the thin metal was still transparent for some of the light. This was not the case when the metal thickness was increased to 2000Å. In the case of thin metal devices, the background current was subtracted from the total current to evaluate the diffusion lengths. The same diffusion lengths (within 10%) were found as on the devices with thick metal on the same wafers.

Various implant conditions did not affect the diffusion length results. However, whenever the implant depth reached the $Si_{1-x}Ge_x$ layer, an increased leakage current in base-collector diode characteristics was observed at room temperature ($\sim$ 100nA/1V). This was probably due to implantation damage in $Si_{1-x}Ge_x$. Enhanced implantation damage in $Si_{1-x}Ge_x$ relative to that in Si for similar implantation conditions has been reported [117]. If the n^+ region did not reach the $Si_{1-x}Ge_x$ layer, leakage in p–n junctions was negligible (< 1nA/1V). However, if the p–n junction is within the top Si layer and the collecting junction does not reach the $Si_{1-x}Ge_x$ layer, the thin p^+-Si layer between the $Si_{1-x}Ge_x$ channel and the n^+collector presents an additional barrier for electron transport resulting in lower collector current levels. However, if the barrier thickness is small (a few hundred Å) compared to the lateral basewidth (which was always the case in our devices), the collector currents at different basewidths should still scale as $\exp(-w_B/L_n)$, so that the same extracted L_n is found. Neither the Si-cap thickness nor the processing variations affected the L_n measurements within the experimental error, so parallel transport in Si cap layer probably did not affect the results.

The room temperature results are summarized in Fig. 6.8. Also shown in the figure are the results for Si reported by Swirhun [97] and Leu and Neugroschel [118].

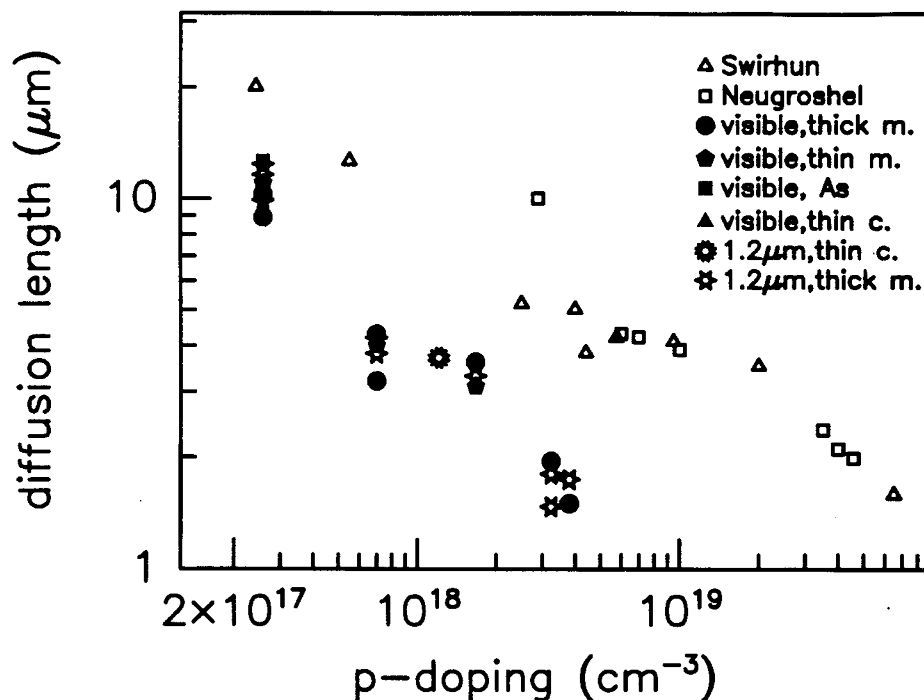

Figure 6.8: Room temperature diffusion length vs.doping in $Si_{0.8}Ge_{0.2}$, published Si data is also shown

For heavily doped Si (above $\sim 2 \times 10^{19}$ cm^{-3}), the decrease in measured diffusion lengths is attributed to Auger recombination. At lower doping levels, the lifetimes measured in Si from processed samples (reflected in the plotted Si diffusion lengths of Fig. 6.8), were well below the Auger limit, most likely caused by Shockley-Read-Hall (SRH) or trap-assisted Auger processes [97, 118]. Both SRH and trap-assisted Auger recombination are mediated by recombination centers in the bandgap so the measured minority carrier parameters reflect both material and processing quality. Since our samples are all doped well below 1×10^{19} cm^{-3} we also expect SRH or trap-assisted Auger processes to dominate. It is clear from Fig. 6.8 that the values obtained for our samples have lower diffusion lengths than similarly doped silicon at room temperature.

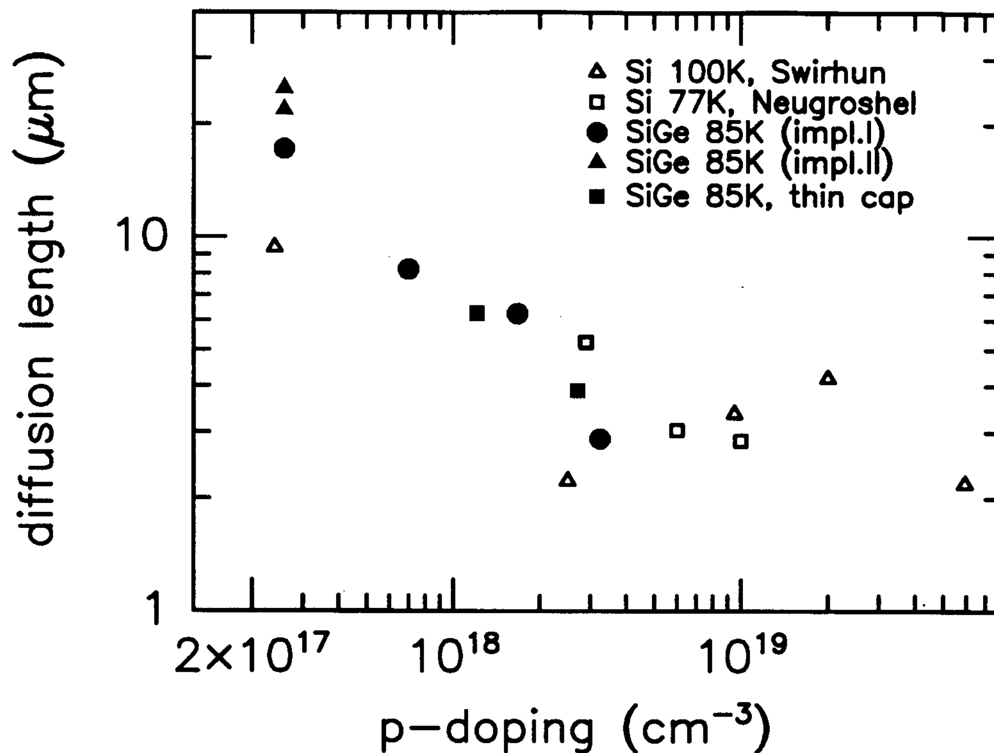

Figure 6.9: Low temperature diffusion length vs.doping in $Si_{0.8}Ge_{0.2}$, also shown published Si data

We have also performed low temperature measurements. Fig. 6.9 shows the $Si_{0.8}Ge_{0.2}$ diffusion length measured at 85K. Also shown for comparison, is the Si data of Swirhun [97] measured at 100K and data of Leu and Neugroschel [118] measured at 77K. There is no sufficient Si data at low temperature published to clearly establish diffusion length vs. doping curve, and the temperature dependence of minority carrier mobility is strongly doping dependent [97], but it is clear from Fig. 6.9 that data points for $Si_{1-x}Ge_x$ lie near the published Si data.

We think that the reason for the diffusion lengths compared to Si at room vs. low temperature is not a bulk $Si_{1-x}Ge_x$ property, but that the room temperature data is affected by surface recombination due to the limited quality of our passiva-

tion oxide. If the effective surface recombination velocity is much larger than we expected, the effective lifetime would be much lower resulting in lower measured diffusion lengths. At low temperature however, due to the better confinment of carriers within $Si_{1-x}Ge_x$ (exponential factor in equation 6.7), the surface recombination becomes less significant and measured diffusion lengths represent true properties of the material. This was confirmed by temperature dependent PL measurements. It has recently been shown [119] that the photoluminescence (PL) from $Si_{1-x}Ge_x$ quantum wells decreases with increasing temperature above 100K due to a low effective lifetime caused by surface recombination at the top Si surface.

To extract minority carrier mobility one still needs to measure the lifetime. If measured at room temperature on the same samples, the true mobility values could be extracted since the same effective lifetime would be measured as that affecting the diffusion length measurements, provided that the surface is passivated in the same manner. One way to measure electron lifetime would be to modulate the light source at a frequency ω, where $\omega \sim 1/\tau$ ($\sim$ 10MHz) and use equation 6.4 to calculate lifetimes from DC and AC diffusion lengths [113] or monitor the transient response in the frequency domain [114]. A more straightforward way would be to measure the change in photoconductivity of the sample in time when illuminated with a short light pulse [112]. Finally, all the samples used in this study exhibited strong PL signal at 77K and 10K. By monitoring the PL decay low temperature lifetime could be measured. The lifetime measurement and extraction of a lateral minority carrier diffusion coefficient vs. doping will be subject of future work.

Note that for HBT modeling the vertical (not lateral as given in this chapter) D_n is needed. The strain moves the four conduction band valleys in the growth plane down with respect to the other two in the growth direction. As a result, the electrons traveling in the growth direction will experience the transverse effective mass $m^* = m_t$ (0.19 in Si) while those in the growth plane will see m^* given by:

$\frac{2}{m^*} = \frac{1}{m_l} + \frac{1}{m_t}$. Assuming that the strain does not affect the band curvatures, one could easily relate vertical and lateral electron mobilities as the ratio of lateral and vertical effective masses.

6.6 Summary

This chapter provides details of $Si/Si_{1-x}Ge_x/Si$ heterostructure design for the best performance of lateral devices to extract minority carrier parameters in strained $Si_{1-x}Ge_x$. The first measurements of the electron diffusion length as a function of p-doping (2×10^{17} cm^{-3} – 4×10^{18} cm^{-3}) in $Si_{0.8}Ge_{0.2}$ are presented. Room temperature results are affected by surface recombination and the diffusion length appears lower than that reported in Si. Effects of the surface recombination are supressed at low temperature due to better confinment of carriers within the $Si_{1-x}Ge_x$ layer. Low temperature diffusion length values (85K) appear similar or slightly higher than reported Si data. This may be due to high quality material (higher lifetimes) or increased minority carrier mobility. Minority carrier lifetime still remains to be measured to extract the electron mobilities.

Chapter 7

Electron Resonant Tunneling in $Si/Si_{1-x}Ge_x$ Heterostructures

7.1 Introduction

The main focus of this thesis has been npn $Si/Si_{1-x}Ge_x/Si$ HBT's, the device in $Si/Si_{1-x}Ge_x$ material system which is the most likely to be exploited in industry in the near future. However, opportunities for novel heterojunction device structures in Si-based material system exist beyond HBT's. One interesting vertical-transport devices is a resonant tunneling structure. In chapter 3 we have used p-type resonant tunneling diodes as a tool to characterize $Si/Si_{1-x}Ge_x$ interfaces. From the application perspective, resonant tunneling devices are very interesting because of their potential high speed performance [120, 121, 122]. The integration of resonant tunneling diodes into transistor structures opens a field of multifunctional devices which can lead to a reduction in circuit complexity and size. This field has advanced much further in III-V's than in the Si-based material system. Since the first resonant tunneling bipolar transistor operating at room temperature was demonstrated [123], such applications as a multiple state memory [124, 125], a parity generator [126], and a frequency multiplier [127] have been demonstrated in III-V's.

7.2 Device fabrication

In $Si/Si_{1-x}Ge_x$ material system, the resonant tunneling of holes has been extensively studied [72, 73, 74], but the electron resonant tunneling has not received much attention, except for the single report of Ismail et al. [75]. This is mainly due to the energy band configuration, namely the relatively large valence band offset of a strained $Si_{1-x}Ge_x$ layer grown on Si substrate, as explained in chapter 2. To achieve the electron resonant tunneling, a certain offset in the conduction band is needed. This can be accomplished by exploiting a strained Si/relaxed $Si_{1-x}Ge_x$ heterojunction grown on a relaxed $Si_{1-y}Ge_y$ buffer on top of a <100> Si substrate. Such a structure requires a capability of growing high quality, n-type doped, relaxed $Si_{1-x}Ge_x$ layers. In these structures, Si layers are subjected to tensile strain. The strain causes splitting of the conduction bands, such that the four valleys in the growth plane move up in energy, while the two valleys in the growth direction move down. The two valleys form the conduction band edge in Si which is actually lower than that of the surrounding SiGe. The conduction band offset is expected to be $\sim$ 200meV for $Si_{0.65}Ge_{0.35}/Si$ heterojunction, while the splitting of conduction bands is predicted to be $\sim$ 230meV, calculated according to the model of Van de Walle and Martin [35]. The two-fold degenerate lowest band in the strained Si has a heavy mass in the growth direction ($m_z \approx 0.98$). Due to the large conduction band splitting it is expected that only the heavy electrons will be involved in the tunneling process. The schematic conduction band diagram of the structure at zero bias is shown in Fig. 7.1.

The structures were grown by RTCVD on a <100> n-type silicon substrate. A 0.5μm-thick continuously graded $Si_{1-x}Ge_x$ layer was grown at 625°C, up to x = 0.35. On top of the graded layer a $1\mu m$-thick, n-type doped $Si_{0.65}Ge_{0.35}$ buffer was grown, doped $\approx 7\text{x}10^{18}cm^{-3}$ using phosphine as the dopant source. The growth was followed by an in situ anneal at 800°C for an hour, which provided a fully relaxed "substrate"

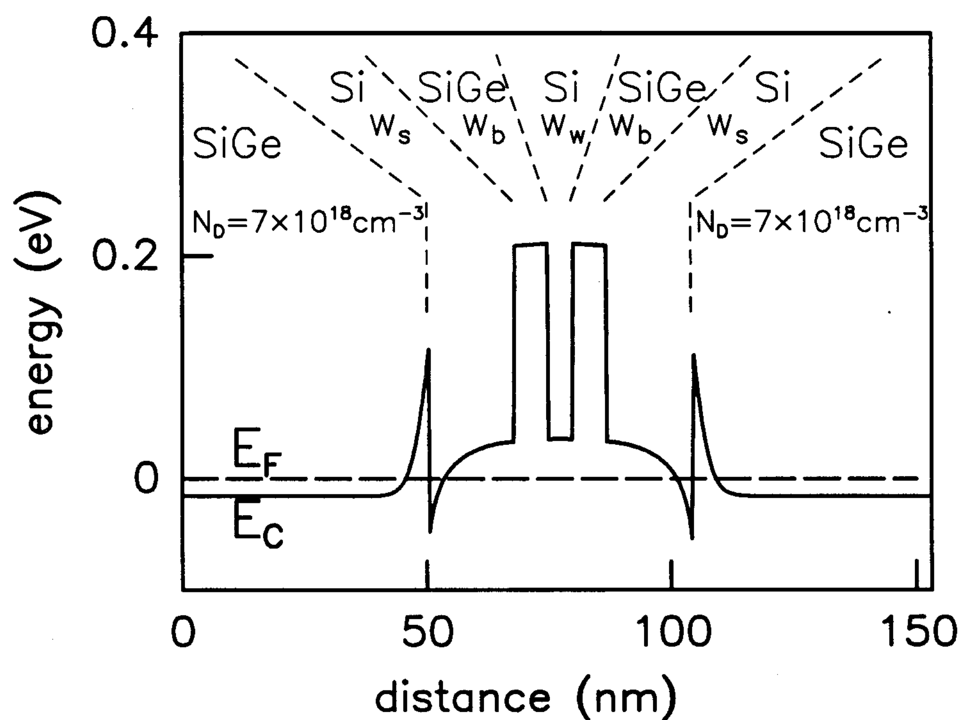

Figure 7.1: Schematic conduction band diagram at zero bias. Also shown are the different layers: silicon spacers, $w_s = 175Å$; $Si_{0.65}Ge_{0.35}$ barriers, $w_b = 40 - 70Å$; and Si well, $w_w = 20 - 50Å$.

for the double barrier structure. Undoped 175Å wide Si spacers were grown to prevent dopant diffusion into the barriers and the well. $Si_{0.65}Ge_{0.35}$ barriers were grown at 625°C, with the thicknesses nominally varying from 40 to 70Å on different samples. The silicon quantum well was grown at 700°C, and its width varied from 20 to 50Å. On top of the double barrier structure another n-type $Si_{0.65}Ge_{0.35}$ ($\approx 0.1\mu m$) layer was grown, with the top 300Å very heavily doped ($\approx 10^{20}cm^{-3}$) to provide ohmic contacts. The devices were fabricated by a simple mesa process. The metal (Ti/Al) was used as a mesa mask and the contacts were annealed for 20 minutes in forming gas at 350°C. The mesa sidewalls were not passivated. The resulting device structure is shown in Fig. 7.2. The device area varied from 60×60 to $130 \times 130\mu m^2$.

7.3 Results

Symmetric resonant tunneling of electrons for various well and barrier widths was observed for the first time [128]. In earlier work, only a single broad peak for one positive bias was observed [75]. The peak-to-valley ratios of 2 were observed for the sharpest resonance at 4.2K for the devices with the well widths of 25Å and barrier widths of 60Å, as seen from Fig. 7.3. In the I-V curves resonant features start to appear at about 225K (at 240K in dI/dV curves). At 150K (labeled (b) in Fig. 7.3) the two distinct peaks are obvious. When the temperature is further decreased the higher bias peak (labeled HE_0) becomes sharper due to the suppression of the background current (thermionic current component and scattering effects), but the lower one (labeled X) becomes weaker, completely disappearing at low temperatures (d). At 4.2K the peak-to-valley ratio is at its largest value for the higher bias resonance. Devices with different well and barrier widths all exhibit similar temperature behaviour, except that the number and strengths of resonances varies. All of the resonances except the lowest are strongest at 4K and decrease with an increase in temperature. The

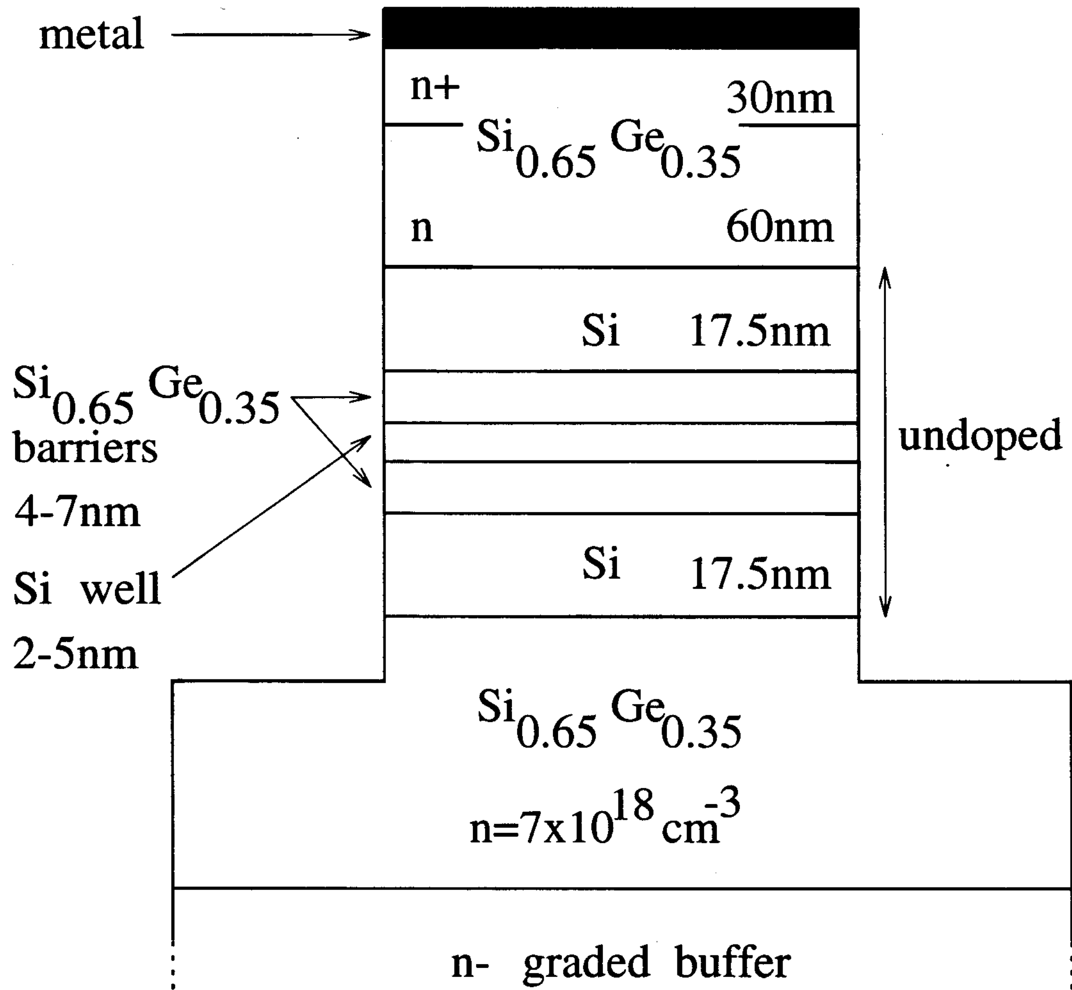

Figure 7.2: RTD device structure

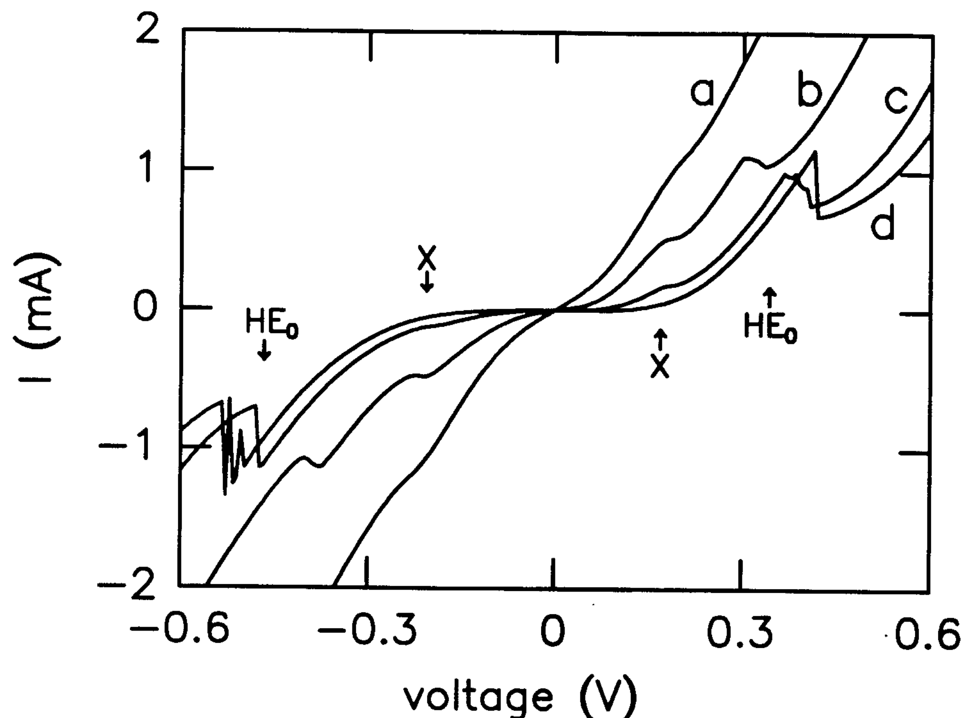

Figure 7.3: I-V curves of a device with 25Å well and 60Å barriers (area=70 × 70μm^2) at various temperatures: (a) 220K, (b) 150K, (c) 80K, (d) 4.2K.

lowest energy resonance is not visible below T $\approx$ 50K, (even in dI/dV), but rapidly increases in strength up to 120-140K, above which it slowly disappears into the increasing background current. The peak current density of the higher bias peak of the device shown in Fig. 7.3 at 80K is 20A/cm^2, and increases to 800A/cm^2 as the barrier width is reduced to 40Å (the well width remains constant). The devices with wider wells exhibit more resonant peaks, as expected, due to lower states in the well, but the resonances are weaker compared to the narrower well devices (25Å). Fig. 7.4 shows I-V and dI/dV curves for a device with a 50Å well and 70Å barriers, at 80K. There are four distinct resonances observed in the dI/dV curve. The resonant features are symmetric for positive and negative biases (with respect to the top layer in the structure). In general, the position of resonances for opposite bias polarities

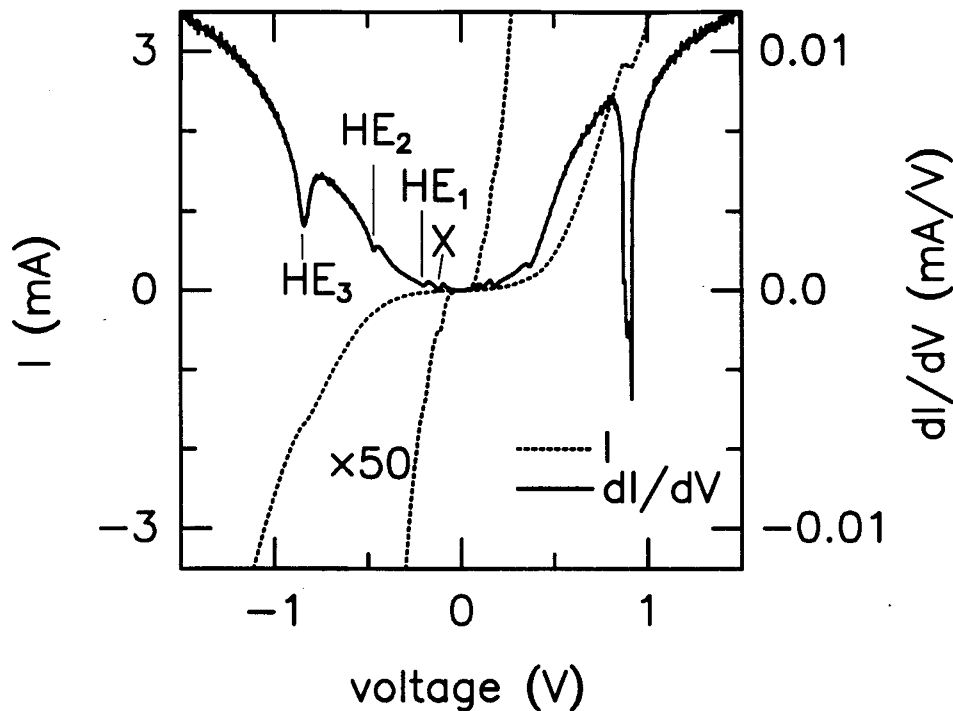

Figure 7.4: Typical I-V and dI/dV-V curves of a 50Å well/70Å barriers device (area=100 × 100μm^2) with four distinct resonances at 80K

are within 15% for all devices. The symmetric position of the resonances for positive and negative biases implies symmetric spacer thicknesses (within 25Å), which implies negligible phosphorous segregation at the lower n^+SiGe/Si interface.

We have used a simple first order model to relate resonant features to the calculated states in the quantum well, assuming an electron effective mass of $0.98m_o$, no charge buildup in the well, no voltage drop in the emitter and full depletion of the collector spacer. For example, for device with a 50Å well and 70Å barriers, the calculated bias positions corresponding to the ground state, first, second, and third excited state in the well ($HE_0 - HE_3$) are 42, 165, 369, and 627mV, respectively. The observed bias positions (positive and negative) of the four distinct resonances in the dI/dV curve at 80K were: 112-120, 162-180, 365-400, and 700-900mV. The three higher bias reso-

nances are easily associated with the tunneling to the first three excited levels of the quantum well (HE_1, HE_2 and HE_3), but the lowest bias resonance does not fit into the model. Since the ground state energy in the well (HE_0) is calculated to be only 11meV, tunneling to this state might indeed not be observed, because of too high a Fermi level in the emitter, explaining the absence of the expected 42mV peak, but not the origin of the 112-120mV peak. Similar calculations on the samples with different barrier and well widths gave similar results. A summary of samples is given in Table 7.1. In devices with narrower wells and hence higher HE_0 states, the HE_0 state was observed, but a lower lying anomalous peak was still also seen (as in the devices of figures 7.3 and 7.4). Therefore both, the calculation of resonance positions and the temperature behaviour suggest a different origin of the lowest energy resonance. To our knowledge, this is the first time that such an anomalous temperature dependence of a resonant peak has been reported. A first possible explanation for this behaviour involves the quantization of levels in the accumulation layer expected to form in the emitter (assuming 2-D to 2-D tunneling). At low temperature, only the ground state in the emitter would be occupied, but at high temperatures tunneling could also occur from thermal electrons in the first excited state, yielding a low bias replica from the emitter ground state resonance. However, the shape of I-V curves (figures 7.3 and 7.4) strongly suggests 3-D to 2-D tunneling process (not 2-D to 2-D) [129, 130]. Tunneling through a defect-state, since there is a relatively high concentration of defects present in structures grown on relaxed $Si_{1-x}Ge_x$ buffer layers ($\sim 1 \times 10^7$ cm^{-2}), would not explain the temperature behaviour of the anomalous resonance. Finally, we propose a phonon-absorption-assisted resonant tunneling model to explain the temperature behaviour of the lowest-bias resonance [131].

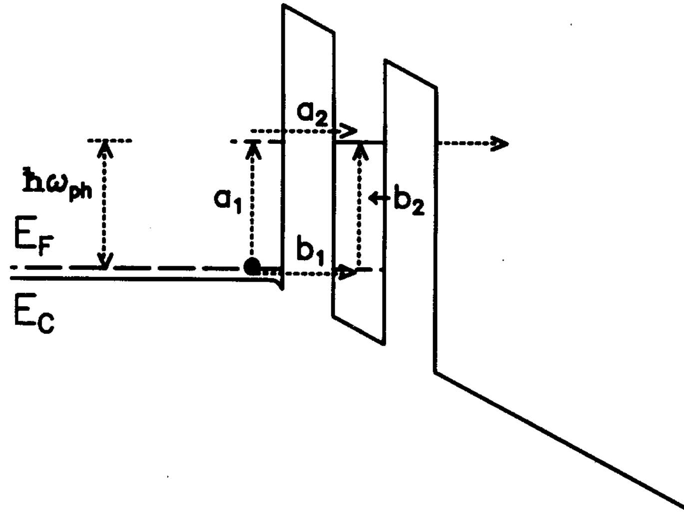

Figure 7.5: Schematic diagram of phonon-absorption-assisted tunneling indicating phonon absorption prior to tunneling (path $a_1 - a_2$) and after tunneling (path $b_1 - b_2$).

7.4 Phonon-absorption-assisted model

There has been evidence of phonon-*emission*-assisted tunneling in III-V material system [132]. In this process an electron can tunnel into the well by emitting an LO-phonon near the zone center. Therefore, at higher bias a small replica of the elastic resonance appears in the I-V curve. The voltage difference between the position of the elastic resonance and the phonon-replica is related to the LO-phonon energy.

We propose a model for the low bias feature involving electron tunneling via phonon *absorption,* as illustrated in Fig. 7.5. An electron of energy E in the emitter absorbs a phonon to acquire energy $\hbar\omega_{ph}$ to tunnel into the well state ($E + \hbar\omega_{ph}$). As explained earlier, the conduction band in strained silicon is twofold degenerate,

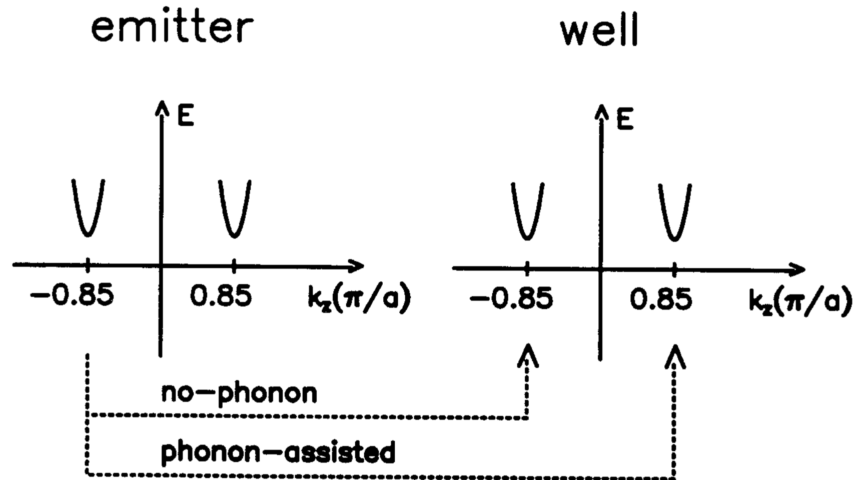

Figure 7.6: Schematic diagram illustrating direct and phonon-assisted electron tunneling processes in SiGe/Si material system. Phonon-assisted process: $\Delta k_z \approx q \approx 2 \times 0.85\pi/a + G \approx 0.3\pi/a$

with the heavy electron effective mass along the growth direction (z-axis). The two conduction band minima in silicon lie at Δ−point ($k_z \approx \pm 0.85\pi/a$). This enables phonon-assisted scattering from one valley to another, as illustrated in Fig. 7.6. The transverse momentum is conserved while the absorbed phonon contributes to k_z, with the phonon momentum q equal to $2k_z - G \approx 0.3\pi/a$ (where G is the reciprocal lattice vector). Since the optical phonons have relatively high energies ($\approx$ 62meV at $q = 0$ for Si [86] we expect acoustic phonons to be involved in this process rather than optical. For a transverse acoustic (TA) phonon in silicon, the energy corresponding to $q = 0.3\pi/a$ is $\approx$ 13meV [86]. This would give a peak in the I-V curve corresponding

to an energy of 13meV below the true quantum well state. Given the thicknesses of different layers in the structure, the same first order model used earlier to relate energy and voltages for a device with 50Å well and 70Å barriers predicts a shift in bias position of 50mV. For the 50Å well device described earlier, the expected position of the low bias replica of the HE_1 state is then $165 - 50 = 115$mV, in surprisingly good agreement with the measured biases of 112-120mV for the anomalous peak. This feature is not observed for higher resonant levels, possibly due to the significant increase in the background current at higher biases.

A careful study of the temperature dependence supports the phonon-absorption hypothesis. The total size of the resonance should be proportional to the number of phonons available (n_{ph}) to be absorbed:

$$I \propto n_{ph} \propto \frac{1}{e^{\hbar\omega_{ph}/k_bT} - 1} \tag{7.1}$$

where $\hbar\omega_{ph}$ is the phonon energy. This qualitatively explains the disappearance of the peak at low temperatures. A quantitative analysis was performed by separating the background current by fitting the I-V data at different temperatures to a third-order piecewice-polynomial curve, excluding the data points at the resonance. The edge bias points of the excluded interval at the resonance were manually selected so that the background current fit exhibited no resonances or features. The actual data and fitted background I-V curves for a 50Å well device at three different temperatures are shown in Fig. 7.7. Fig. 7.8 shows the resulting lowest-bias-resonance strength vs. inverse temperature for different devices. Curves (a) and (b) are data for a device with 25Å well, for positive and negative biases, and curve (c) is data for a 50Å well device. The error in the data points due to the background fitting procedure is expected to be less than 10%. The data points were then fitted to equation 7.1 with the phonon energy and a vertical scaling constant as adjustable parameters, yielding the dashed lines in Fig. 7.8. The resulting phonon energies of 14meV, 16meV and 12meV for

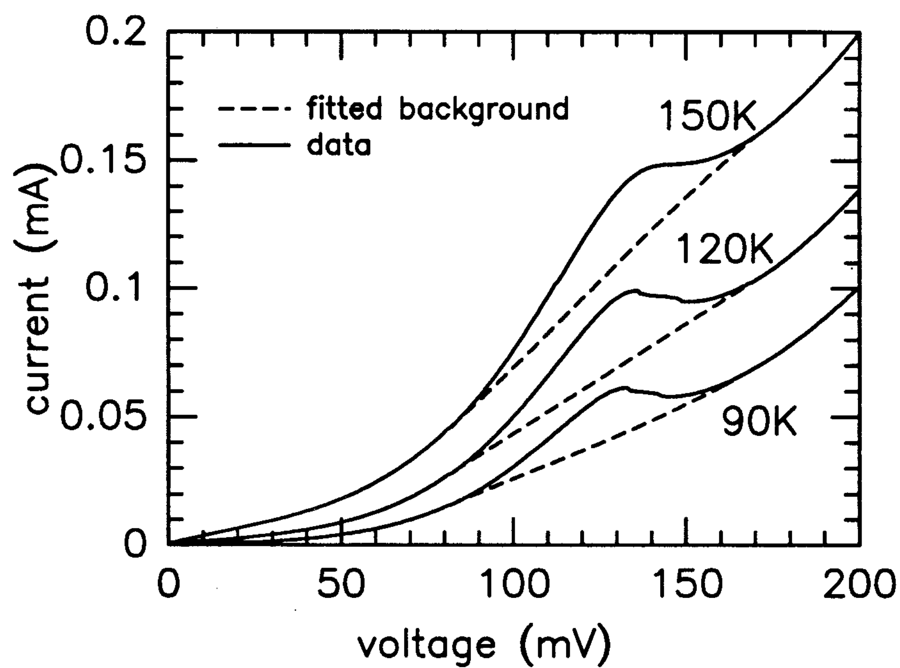

Figure 7.7: I-V curves of the lowest energy resonance for a 50Å well device at three different temperatures

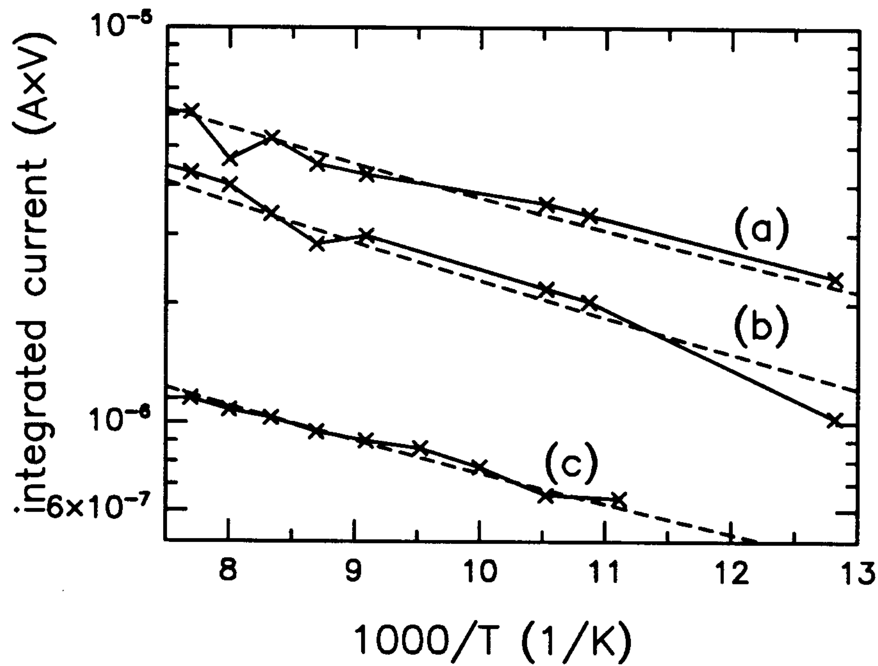

Figure 7.8: Integrated tunneling current for the lowest energy resonance vs. 1000/T for: (a) 25Å well device, positive bias, (b) 25Å well device, negative bias, (c) 50Å well device, positive bias. The dashed lines are fits to phonon population curves (a) $\hbar\omega = 14meV$, (b) $\hbar\omega = 16meV$, (c) $\hbar\omega = 12meV$

(a),(b) and (c), respectively, are very close to predicted 13meV for the TA-phonon in silicon with $q = 0.3\pi/a$, and strongly support the phonon-absorption-assisted model as the origin of the lowest bias resonance.

Any two-step process, such as phonon absorption and tunneling, requires that the system pass through an intermediate state. In the case of the phonon-absorption-assisted tunneling process the electron may become "hot" by absorbing the phonon (step a_1 in Fig. 7.5) prior to tunneling (step a_2), so that the intermediate state could be a true existing state in the conduction band of the emitter with a finite lifetime. This is in contrast to tunneling before the phonon absorption (steps b_1 and b_2 in Fig. 7.5) or to any path for phonon-emission-assisted tunneling where the intermediate state would be only a "virtual" state. Furthermore, after absorbing a phonon (a_1), an electron will see a substantially lower tunneling barrier height than following the $b_1 - b_2$ path or any path for phonon emission. Therefore, it is reasonable that transitions through phonon absorption, when allowed by the energy and momentum conservation rules, are more favorable than phonon-emission related transitions. This could explain why no high-energy replicas corresponding to phonon-emission were observed in our samples and why the relative strength of such a resonance is comparable to the true elastic resonance through the level with which it is associated.

A unique feature of the strained $Si/Si_{1-x}Ge_x$ system is that low energy (and hence plentiful) acoustic phonons may be involved due to the momentum transfer between the degenerate conduction band minima. In a material system with one band minimum, only high energy zone center optical phonons would be allowed, making such phenomenon much less likely to occur due to a lower number of phonons. That is a possible reason why phonon-absorption-assisted features have not been observed for holes in Si/SiGe or in III-V material systems.

7.5 Summary

The first symmetric electron resonant tunneling diode, a novel vertical transport device in $Si/Si_{1-x}Ge_x$ material system, has been demonstrated. This confirms high quality of RTCVD epitaxial layers and possibly opens a new area of multifunctional devices to be researched. An anomalous temperature dependence of a low bias resonance has been observed. Both the comparison of observed resonances with the calculated states in the well and the temperature behaviour are consistent with a model of phonon-absorption-assisted tunneling.

sample number	well width (Å)	barrier width (Å)	spacer width (Å)	calculated bias (mV)	observed bias (mV)	temperature dependence	assignment of observed resonance
1072 center	50	70	175	42 (HE_0) 165 (HE_1) 369 (HE_2) 627 (HE_3)	112-120 162-180 365-400 700-900	anomalous o.k. o.k. o.k.	X HE_1 HE_2 HE_3
1072 center	40	65	175	65 (HE_0) 252 (HE_1) 552 (HE_2)	160-170 220-250 600-800	anomalous o.k. o.k.	X HE_1 HE_2
1072 edge	15-25	40-60	125-175		180-250 300-450	anomalous o.k.	X HE_0
1149 center	30	50	175	 118 (HE_0) 456 (HE_1)	50-55 95-120 426-515	anomalous o.k. o.k.	X HE_0 HE_1
1149 edge	10-25	30-50	100-175		150-300 200-500	anomalous o.k.	X HE_0

Table 7.1: Summary of RTD samples

Chapter 8

Conclusions and Suggestions for Further Research

8.1 Conclusions

The research leading to this thesis mainly focussed on $Si/Si_{1-x}Ge_x/Si$ HBT's: issues related to process integration and experimental determination of parameters critical for accurate DC device modeling and design.

The interest in $Si/Si_{1-x}Ge_x/Si$ HBT's lies in the potential to fabricate high speed devices and circuits, since the HBT structure allows increased base dopings to reduce base sheet resistance and graded germanium profiles to reduce base transit times. Low intrinsic device delay (high f_T), low parasitic base resistances, low parasitic capacitances, and optimized load are prerequisites for high speed circuit performance. When integrated into Si technology, processing needs to be adjusted to reduced thermal cycles (to below 800°C) to prevent strain relaxation and minimize dopant diffusion in the base.

All the samples in this work were grown by RTCVD. The quality of epitaxial material and interfaces was studied in a wide pressure range, by means of x-ray reflectivity, photoluminescence and electrical performance of p-type resonant tunneling diodes. An interface roughness of below 5Å was established for high quality epitaxial layers grown at low pressure.

A heavily doped base and a heavily doped emitter in a bipolar transistor lead to

a p^+–n^+ junction. Tunneling currents in p^+–n^+ base-emitter junction could cause a severe increase in the base current. The doping on the lighter doped side of the junction should not exceed 5×10^{18} cm^{-3} in order not to cause significant tunneling. Both tunneling, and boron diffusion can be controlled by carefully designed undoped spacer layers within the $Si_{1-x}Ge_x$ base.

From the room temperature collector current measurements, bandgap narrowing in heavily doped $Si_{1-x}Ge_x$ layers was extracted in a wide range of p-type dopings and germanium concentrations for the first time. An empirical model for the effective bandgap narrowing relevant for the minority carrier transport in the base was presented. The heavy doping contribution to the effective bandgap narrowing is lower than that in Si, due to the strain-induced splitting of the bands which pushes the Fermi level further into the valence band for a given hole concentration. Furthermore, the design trade-off between the base sheet resistance and gain was clearly presented.

The minority carrier diffusion length was extracted for the first time in p-type $Si_{1-x}Ge_x$ as a function of doping from the photocurrent measurements on optimized lateral devices at room temperature and 85K.

Finally, a novel vertical transport device in the Si-based material system, a symmetric electron resonant tunneling diode was demonstrated for the first time. The anomalous temperature behaviour of the lowest bias resonance was explained by phonon-absorption-assisted model.

8.2 Suggestions for future work

This thesis gives the first empirical model of bandgap narrowing (due to Ge and heavy doping) in strained $Si_{1-x}Ge_x$ layers obtained from collector current measurements. It would be interesting to observe bandgap narrowing as a function of germanium

concentration and p-type doping in $Si_{1-x}Ge_x$ by optical measurements, such as photoluminescence, and compare it to the electrical results. In this way the relationship between the "true" bandgap narrowing and the effective one could be accurately determined and compared to Si.

The minority carrier lifetime in p-$Si_{1-x}Ge_x$ still remains to be measured. Combined with the diffusion lenght measurements presented in this work, this could lead to the first measurement of minority carrier mobility in strained $Si_{1-x}Ge_x$, a parameter critical for accurate collector current modeling.

The focus of this work has been p-type material since the base in npn HBT is a heavily p-type doped $Si_{1-x}Ge_x$ layer. However, for various device applications, such as pnp HBT for example, n-type material also deserves to be studied.

The integration of HBT's with resonant tunneling structures into multifunctional devices still needs to be demonstrated in $Si/Si_{1-x}Ge_x$ material system. This might be easier to accomplish for a pnp HBT where the double barrier for hole transport could be integrated within the vertical structure of the device (in base-emitter space charge region or in the base, for example). Integration of electron resonant tunneling structures requires further improvement in the relaxed buffer layers, in terms of defect densities and high quality material with high minority carrier lifetimes.

Research on other materials, such as silicon-carbide or silicon-germanium-carbon alloys extends the field of heterojunctions on silicon and among other, possible bipolar device applications.

Finally, $Si/Si_{1-x}Ge_x/Si$ HBT's have been pushing the limits of high speed device performance and integration into silicon bipolar technology. How far this trend will continue still remains to be seen.

Appendix A

Growth and Processing Details

This appendix provides growth details and run-sheets for typical samples of each chapter in this thesis. It also gives processing details for p and n-type resonant tunneling diodes.

A.1 Graded base HBT samples

Samples in this section are related to chapter 2. Graded base HBT test samples (#758 and #759) were grown on n-type (30-60 Ωcm) <100> Si substrates. The standard "clean + buffer" initial sequence was grown prior to base and emitter HBT layers. The 6 min. high temperature buffer layer was not intentionally doped. All layers were grown at 6 torr with constant H_2 flow of 3slpm and DCS flow of 26sccm. The growth sequence for sample #759 is given in Tab. A.1.

AT&T samples (#996–1002, #1011–1018) were grown on patterned wafers without the high temperature buffer layer (only 30 sec clean at 1000°C), and a thin (~180Å) Si layer was grown at 700°C prior to base layer growth. These samples only had 500–700Å (105 sec at 800°C) emitter layer doped $\sim 1 \times 10^{18}$ cm^{-3} (PH_3 flow of 2.5 sccm).

Table A.1: HBT sample #759, base and emitter growth

time (sec)	temperature (°C)	GeH_4 (sccm)	B_2H_6 (sccm)	PH_3 (sccm)	comment
					base layer:
134	625	87	0		18%, 150Å spacer
134	625	87	335		
50	625	77	300		5×10^{19} cm^{-3}, 300Å
57	625	68	265		
64	625	59	232		
75	625	50	0		
91	625	41	0		150Å spacer
115	625	32	0		12%
10	625	0	0		purge
					emitter layer:
60	800	0	0	2.5	1×10^{18} cm^{-3}, 400Å
390	800	0	0	25	1×10^{19} cm^{-3}, 2600Å

A.2 Samples for interface roughness study

The growth sequence of sample #1334 is given as an example of a sequence where the $Si_{1-x}Ge_x$ layer is grown at pressure above 6 torr (Tab. A.2). The $Si_{1-x}Ge_x$ layer growth followed the standard high–temperature sequence. DCS flow was constant at 26sccm and not interrupted between layers.

The details of the growth of sample #1432 are also given (Tab. A.3). This is the 20-period superlattice sample used for XRD characterization of the low-pressure and

Table A.2: XRR and PL sample #1334, $Si_{1-x}Ge_x$ and Si cap layer growth

time (sec)	temperature (°C)	pressure (torr)	H_2 (slpm)	GeH_4 (sccm)	comment
60	1000	6	3		
40	700	6	3		
110	625	6→60	3→4→3		stabilize pressure
75	625	60	3	100	$Si_{0.7}Ge_{0.3}$, 250Å
60	625	60	3	0	
300	700	60	3	0	Si cap

low-temperature interfaces.

A.3 P-type resonant tunneling diodes

P-type resonant tunneling structures (#1297, #1336, 6 torr; #1337, 60 torr; and #1374, 220 torr) were grown on p-type (∼ 30Ωcm) <100> Si substrates. The cleaning step consisted of a 2 min. bake at 1000°C and 250 torr. A 5 min. (∼ 1μm thick) buffer layer was doped p-type (B_2H_6 (10 ppm in H_2) flow of 50 sccm). The symmetric, undoped double-barrier structure consisted of a strained $Si_{1-x}Ge_x$ well sandwiched between Si barriers and $Si_{1-x}Ge_x$ spacer layers which were separating the double-barrier structure from the doped emitter/collector Si regions. All the Si layers were grown at 700°C and $Si_{1-x}Ge_x$ layers at 625°C. Si doped layers were doped $2-5\times10^{19}$ cm^{-3}. The top layer was a p^+contact Si layer. The growth sequence of sample #1297 is given as an example (Tab. A.4).

Table A.3: Growth details for superlattice sample #1432

	temperature (°C)	Si carrier flow (sccm)	GeH_4 flow (sccm)	growth rate (Å/min.)
Si layer	625	silane (0.4% in H_2): 250	-	18.8
$Si_{0.8}Ge_{0.2}$	550	DCS: 26	100	4.6

A.4 Flat–base HBT samples

Flat-base HBT samples with uniform B and Ge concentrations were used in chapter 5 to study the minority and majority carrier properties in strained $Si_{1-x}Ge_x$. Chapter 5 provides the list of samples (Tab.5.1). Collectors in these samples were doped via outdiffusion from the n-type doped high–temperature buffer layer. The growth sequence, including the n-buffer, of sample #934 is shown as a typical example (Tab. A.5).

A.5 Lateral SiGe channel devices

The structures designed to study minority carrier parameters in strained $Si_{1-x}Ge_x$ are discussed in chapter 6, and a list of samples is provided (Tab.6.1). The layers were grown on p-type (8-60Ωcm) <100> Si substrates. The high temperature buffer in these structures was thick ($\sim 3\mu m$), and p^+doped (500 sccm B_2H_6 flow). The growth sequence of sample #1570 of the layers following the p^+buffer is shown as a typical example (Tab. A.6).

Table A.4: Sample #1297, p-type RTD

time (sec)	temperature (°C)	GeH_4 (sccm)	B_2H_6 (sccm)	comment
60	1000		50	
600	700		50	p–Si
45	625			temp. stabilize
60	625	200		$Si_{0.75}Ge_{0.25}$ spacer, 160Å
10	625			purge
100	700			barrier, 50Å
45	625			temp. stabilize
15	625	200		$Si_{0.75}Ge_{0.25}$ well, 40Å
10	625			purge
100	700			barrier, 50Å
45	625			temp. stabilize
60	625	200		$Si_{0.75}Ge_{0.25}$ spacer, 160Å
10	625			purge
600	700		50	p–Si
600	700		450	p^+–Si

A.6 N-type resonant tunneling diodes

Double-barrier structures for electron resonant tunneling were grown on relaxed, graded $Si_{1-x}Ge_x$ buffer layers (see chapter 7), as developed by C.W. Liu. The growth sequence (following the high–temperature buffer) for sample #1072 is given here (Tab. A.7).

Table A.5: Sample #934, flat-base HBT

time (sec)	temperature (°C)	GeH_4 (sccm)	B_2H_6 (sccm)	PH_3 (sccm)	comment
60	1000				clean
600	1000			2.5	n-buffer
~ 600	cold				
240	1000			-	collector
60	700				
40	625				temp. stab.
300	625	50			BC $Si_{0.86}Ge_{0.14}$ spacer
600	625	50	400		$\sim 1 \times 10^{20}$ cm^{-3} base
300	625	50			BE $Si_{0.86}Ge_{0.14}$ spacer
10	625				purge
450	800			2.5	emitter

A.7 Processing of resonant tunneling diodes

All of the resonant tunneling diodes of chapter 7 (n-type) and most of the RTD devices of chapter 3 (p-type) were processed by a simple mesa process involving only one photolitographic step. P-type devices were also processed by a three-step wet-etch process There was some differencies in the observed I-V curves between the devices from the same wafer processed in different ways (peak-to-valley ratio, peak position), although this might not be process related but due to layer nonuniformity across the wafer. Both of the processes are described. Short anneals (conditions given below) improved peak-to-valley ratios on some devices and moved the peak position towards a slightly lower bias (probably due to lower contact resistance). All the devices with

Table A.6: Sample #1570, lateral transport device

time (sec)	temperature (°C)	GeH_4 (sccm)	B_2H_6 (sccm)	comment
420	800		210	$\sim 1 \times 10^{19}$ cm^{-3} Si
30	700		35	
180	625		→2.5	set flow
360	625	100	2.5	p–$Si_{0.8}Ge_{0.2}$ channel
45	625		→210	set flow
312	800		210	$\sim 1 \times 10^{19}$ cm^{-3} Si cap
7	800		-	

only Al metalization (no Ti) did not survive the 10min anneal at 400°C (probably due to Al spiking).

Singe-step process

- initial RCA clean
- metal evaporation (e-beam evaporator: 500Å Ti + 2000Å Al or just 2500Å Al in some cases)
- photolitography (define mesas)
- metal etch (Al etch + HF : $H_20(1:100)$ for Ti)
- plasma etch using metal mask (SF_6 only 15sccm, 150mtorr, 100W, 0.4min $\sim$ 5000-6000Å)
- photoresist strip
- clean HF : $H_20(1:50)$, 30 sec
- Al evaporation on the back or in the corner for the bottom electrode

- anneal (on some samples, 400°C, 10-15 min, N_2)

Wet-etch process

- initial clean
- photolitography (define mesas)
- wet mesa etch (5000-6000Å)
- photoresist strip
- photolitography (for bottom conatact lift-off)
- clean $HF : H_20(1 : 10)$, 30 sec
- metal evaporation (e-beam evaporator: 3000Å Al)
- lift-off
- RTA (450°C, 5 min, N_2)
- photolitography (for top conatact lift-off)
- clean $HF : H_20(1 : 10)$, 30 sec
- metal evaporation (e-beam evaporator: 3000Å Al)
- lift-off
- RTA (380°C, 3 min, N_2)

Table A.7: Sample #1072, n-type RTD

time (sec)	temperature (°C)	GeH_4 (sccm)	PH_3 (sccm)	comment
60	1000			
40	700			
40	625			
3000	625	0–35	14	1-10%, ~1000Å
2400	625	35–100	14	10-20%, ~2500Å
780	625	100–450	14	20-35%, ~2600Å
1500	625	450	14	$Si_{0.65}Ge_{0.35}$, 7500Å
3600	800			anneal
45	625			set temp.
10	625	450		
350	700			Si spacer, 175Å
45	625			set temp.
14	625	450		$Si_{0.65}Ge_{0.35}$ barrier, 70Å
10	625			purge
100	700			Si well, 50Å
45	625			set temp.
14	625	450		$Si_{0.65}Ge_{0.35}$ barrier, 70Å
10	625			purge
350	700			Si spacer, 175Å
45	625			set temp.
120	625	450	14	n–$Si_{0.65}Ge_{0.35}$, 600Å
60	625	450	150	n^+–$Si_{0.65}Ge_{0.35}$ contact layer

Appendix B

Publications and Presentations Resulting from this Thesis

1. Ž. Matutinović Krstelj, E. Chason, and J. C. Sturm, "Growth pressure effects on $Si_{1-x}Ge_x$ CVD", submitted for publication to J. of Electronic Materials.

2. J. C. Sturm, X. Xiao, Q. Mi, C. W. Liu, A. St Amour, Ž. Matutinović Krstelj, L. C. Lenchyshyn, and M. L. W. Thewalt, "Photoluminescence and Electroluminescence processes in $Si_{1-x}Ge_x$ heterostructures grown by chemical vapor deposition, Mater. Sci. and Eng., B21, 1993, pp. 307-311.

3. Ž. Matutinović Krstelj, V. Venkataraman, E. J. Prinz, and J. C. Sturm, " A comprehensive study of lateral and vertical current transport in $Si/Si_{1-x}Ge_x/Si$ HBT's", Tech. Dig. Int. Elec. Dev. Mtg. 1993, pp. 87-90.

4. Ž. Matutinović Krstelj, E. Chason, J. C. Sturm, "Growth pressure effects on $Si_{1-x}Ge_x$ CVD", Tech. Prog. Elec. Mat. Conf., 39, 1993.

5. Ž. Matutinović Krstelj, C. W. Liu, X. Xiao, and J. C. Sturm, "Evidence of phonon-absorption-assisted electron resonant tunneling in Si/SiGe diodes", J. Vac. Sci. Technol. B, 11, pp. 1145-1148, 1993.

6. Ž. Matutinović Krstelj, C. W. Liu, X. Xiao, and J. C. Sturm, "Symmetric Si/SiGe electron resonant tunneling diodes with an anomalous temperature behaviour", Appl. Phys. Lett., 62, pp. 603-605, 1993.

7. Ž. Matutinović Krstelj, C. W. Liu, X. Xiao, and J. C. Sturm, "Electron Si/SiGe resonant tunneling diodes grown by RTCVD", Proc. Topical Symposium on Silicon Based Heterostructures, Amer. Vac. Soc., 1992.

8. Ž. Matutinović-Krstelj, E. J. Prinz, P. V. Schwartz, and J. C. Sturm, "Reduction of the p^+–n^+ junction tunneling current for base current improvement in Si/SiGe/Si heterojunction bipolar transistors," Proc. Mat. Res. Soc. Symp., 220, pp. 445-450, 1991.

9. Ž. Matutinović-Krstelj, E. J. Prinz, P. V. Schwartz, and J. C. Sturm, "Reduction of p^+–n^+ junction tunneling current for base current improvement in Si/SiGe/Si HBT's", IEEE Electron Device Lett., EDL-12, pp. 163–165, 1991.

10. J. C. Sturm, E. J. Prinz, P. V. Schwartz, P. M. Garone, and Ž. Matutinović-Krstelj, "Growth and transistor applications of $Si_{1-x}Ge_x$ structures by rapid thermal chemical vapor deposition," Proc. First Topical Symposium on Silicon Based Heterostructures, Amer. Vac. Soc., pp. 5-10, 1990.

References

[1] E. Crabbe, B. Mayerson, J. Stork, and D. Harame, "Verical profile optimization of very-high frequency epitaxial Si- and SiGe-base bipolar transistors," *International Electron Devices Meeting Tech. Dig.*, pp. 83–86, 1993.

[2] E. Kasper, A. Gruhle, and H. Kibbel, "The influence of MBE-layer design on the high frequency performance of Si/SiGe HBTs," *International Electron Devices Meeting Tech. Dig.*, pp. 79–82, 1993.

[3] D. Harame, J. M. C. Stork, B. S. Meyerson, K.-J. Hsu, J. Cotte, K. A. Jenkins, J. D. Cressler, P. Restle, E. F. Crabbe, S. S. T. E. Tice, B. W. Scharf, and J. A. Jasaitis, "Optimization of SiGe HBT technology for high speed analog and mixed signal applications," *International Electron Devices Meeting Tech. Dig.*, pp. 71–74, 1993.

[4] H. Kroemer, "Heterostructure bipolar transistors and integrated circuits," *Proc. IEEE*, vol. 70, pp. 13–25, 1982.

[5] S. S. Iyer, G. L. Patton, S. L. Delage, S. Tiwari, and J. M. C. Stork, "Silicon-germanium base heterojunction bipolar transistors by molecular beam epitaxy," *International Electron Devices Meeting Tech. Dig.*, pp. 874–876, 1987.

[6] G. L. Patton, S. S. Iyer, S. L. Delage, S. Tiwari, and J. M. C. Stork, "Silicon-germanium-base heterojunction bipolar transistors by molecular beam epitaxy," *IEEE Electron Device Lett.*, vol. 9, pp. 165–167, 1988.

[7] T. Tatsumi, H. Hirayama, and N. Aizaki, "Si/$Ge_{0.3}Si_{0.7}$/Si heterojunction bipolar transistor made with Si molecular beam epitaxy," *Appl. Phys. Lett.*, vol. 52, pp. 895–897, 1988.

[8] H. Temkin, J. C. Bean, A. Antreasyan, and R. Leibenguth, "Ge_xSi_{1-x} strained-layer heterostructure bipolar transistors," *Appl. Phys. Lett.*, vol. 52, pp. 1089–1091, 1988.

[9] D.-X. Xu, G.-D. Shen, M. Willander, W.-X. Ni, and G. V. Hansson, "n-Si/p-$Si_{1-x}Ge_x$/n-Si double-heterojunction bipolar transistors," *Appl. Phys. Lett.*, vol. 52, pp. 2239–2241, 1988.

[10] D.-X. Xu, G.-D. Shen, M. Willander, W.-X. Ni, and G. V. Hansson, "n-Si/p-$Si_{1-x}Ge_x$/n-Si double-heterojunction bipolar transistors," *IEEE Electron Device Lett.*, vol. 9, pp. 453–456, 1988.

[11] P. Narozny, M. Hamacher, H. Dämkes, H. Kibbel, and E. Kasper, "Si/SiGe heterojunction bipolar transistor with graded gap SiGe base made by molecular beam epitaxy," *International Electron Devices Meeting Tech. Dig.*, pp. 562–565, 1988.

[12] J. F. Gibbons, C. A. King, J. L. Hoyt, D. B. Noble, C. M. Gronet, M. P. Scott, S. J. Rosner, G. Reid, S. Laderman, K. Nauka, J. Turner, and T. I. Kamins, "Si/$Si_{1-x}Ge_x$ heterojunction bipolar transistors fabricated by limited reaction processing," *International Electron Devices Meeting Tech. Dig.*, pp. 566–569, 1988.

[13] C. A. King, J. L. Hoyt, C. M. Gronet, J. F. Gibbons, M. P. Scott, and J. Turner, "Si/$Si_{1-x}Ge_x$ heterojunction bipolar transistors produced by limited reaction processing," *IEEE Electron Device Lett.*, vol. 10, pp. 52–54, 1989.

[14] C. A. King, J. L. Hoyt, and J. F. Gibbons, "Bandgap and transport properties of $Si_{1-x}Ge_x$ by analysis of nearly ideal $Si/Si_{1-x}Ge_x/Si$ heterojunction bipolar transistors," *IEEE Trans. Electron Devices*, vol. 36, pp. 2093–2104, 1989.

[15] J. F. Gibbons, C. M. Gronet, and K. E. Williams, "Limited reaction processing: Silicon epitaxy," *Appl. Phys. Lett.*, vol. 47, pp. 721–723, 1985.

[16] G. L. Patton, D. L. Harame, J. M. C. Stork, B. S. Meyerson, G. J. Scilla, and E. Ganin, "Graded-SiGe-base, poly-emitter heterojunction bipolar transistors," *IEEE Electron Device Lett.*, vol. 10, pp. 534–536, 1989.

[17] E. J. Prinz and J. C. Sturm, "Base transport in near-ideal graded-base $Si/Si_{1-x}Ge_x/Si$ heterojunction bipolar transistors from 150 K to 370 K," *International Electron Devices Meeting Tech. Dig.*, pp. 975–978, 1990.

[18] A. Pruijmboom, J. W. Slotboom, D. J. Gravesteijn, C. W. Fredriksz, A. A. van Gorkum, R. A. van de Heuvel, J. M. L. van Rooij-Mulder, G. Streutker, and G. F. A. van de Walle, "Heterojunction bipolar transistors with SiGe base grown by molecular beam epitaxy," *IEEE Electron Device Lett.*, vol. 12, pp. 357–359, 1991.

[19] T. I. Kamins, K. Nauka, J. B. Kruger, J. L. Hoyt, C. A. King, D. B. Noble, C. M. Gronet, and J. F. Gibbons, "Small-geometry, high-performance, $Si\text{-}Si_{1-x}Ge_x$ heterojunction bipolar transistors," *IEEE Electron Device Lett.*, vol. 10, pp. 503–505, 1989.

[20] G. L. Patton, J. H. Comfort, B. S. Meyerson, E. F. Crabbé, G. J. Scilla, E. de Frésart, J. M. C. Stork, J. Y.-C. Sun, D. L. Harame, and J. N. Burghartz, "75-GHz f_T SiGe-base heterojunction bipolar transistors," *IEEE Electron Device Lett.*, vol. 11, pp. 171–173, 1990.

[21] J. H. Comfort, G. L. Patton, J. D. Cressler, W. Lee, E. F. Crabbe, B. S. Meyerson, J. Y.-C. Sun, J. M. C. Stork, P.-F. Lu, J. N. Burghartz, J. Warnock, G. Scilla, K.-Y. Toh, M. D'Agostino, C. Stanis, and K. Jenkins, "Profile leverage in self-aligned epitaxial Si or SiGe base bipolar technology," *International Electron Devices Meeting Tech. Dig.*, pp. 21–24, 1990.

[22] J. N. Burghartz, J. H. Comfort, G. L. Patton, J. D. Cressler, B. S. Meyerson, J. M. C. Stork, J. Y.-C. Sun, G. Scilla, J. Warnock, B. J. Ginsberg, K. Jenkins, K.-Y. Toh, D. L. Harame, and S. R. Mader, "Sub-30 ps ECL circuits using high-f_T Si and SiGe epitaxial base SEEW transistors," *International Electron Devices Meeting Tech. Dig.*, pp. 297–300, 1990.

[23] D. L. Harame, E. F. Crabbe, J. D. Cressler, J. H. Comfort, J. Y.-C. Sun, S. R. Stiffler, E. Kobeda, J. N. Burghartz, M. M. Gilbert, J. C. Malinowsli, A. J. Dally, S. Ratanaphanyarat, M. J. Saccamango, W. Rausch, J. Cotte, C. Chu, and J. M. C. Stork, "A high performance epitaxial SiGe-base ECL BiCMOS technology," *International Electron Devices Meeting Tech. Dig.*, pp. 19–22, 1992.

[24] A. Gruhle, "MBE-grown Si/SiGe HBT's with high β, f_T, and f_{max}," *IEEE Electron Device Lett.*, vol. 13, pp. 206–208, 1992.

[25] A. Schuppen, A. Gruhle, U. Erben, H. Kibbel, and U. Konig, "90 GHz-f_{max} SiGe heterojunction bipolar transistors," *Device Research Conf. Tech. Dig.*, 1994.

[26] J. H. van der Merwe, "Crystal interfaces. Part I. Semi-infinite crystals," *J. Appl. Phys.*, vol. 34, pp. 117–122, 1963.

[27] J. W. Matthews and A. E. Blakeslee, "Defects in epitaxial multilayers; I. Misfit dislocations," *J. Crystal Growth*, vol. 27, pp. 118–125, 1974.

[28] J. W. Matthews and A. E. Blakeslee, "Defects in epitaxial multilayers; II. Dislocation pile-ups, threading dislocations, slip lines and cracks," *J. Crystal Growth*, vol. 29, pp. 273–280, 1975.

[29] J. W. Matthews and A. E. Blakeslee, "Defects in epitaxial multilayers; III. Preparation of almost perfect multilayers," *J. Crystal Growth*, vol. 32, pp. 265–273, 1976.

[30] R. People and J. C. Bean, "Calculation of critical layer thickness versus lattice mismatch for Ge_xSi_{1-x}/Si strained-layer heterostructures," *Appl. Phys. Lett.*, vol. 47, pp. 322–324, 1985.

[31] R. Braunstein, A. R. Moore, and F. Herman, "Intrinsic optical absorption in germanium-silicon alloys," *Phys. Rev.*, vol. 109, pp. 695–710, 1958.

[32] R. People, "Indirect bandgap of coherently strained $Si_{1-x}Ge_x$ bulk alloys on <001> silicon substrates," *Phys. Rev. B*, vol. 32, pp. 1405–1408, 1985.

[33] R. People and J. C. Bean, "Band alignments of coherently strained Ge_xSi_{1-x}/Si heterostructures on <001> Ge_ySi_{1-y} substrates," *Appl. Phys. Lett.*, vol. 48, pp. 538–540, 1986.

[34] D. V. Lang, R. People, J. C. Bean, and A. M. Sergent, "Measurement of the bandgap of Ge_xSi_{1-x}/Si strained-layer heterostructures," *Appl. Phys. Lett.*, vol. 47, pp. 1333–1335, 1985.

[35] C. G. van de Walle and R. M. Martin, "Theoretical calculations of heterojunction discontinuities in the Si/Ge system," *Phys. Rev. B*, vol. 34, pp. 5621–5634, 1986.

[36] X. Xiao and J. C. Sturm, "Direct evidence by photoluminescence of type-I band alignment for strained $Si_{1-x}Ge_x$ ($x \leq 0.35$) on (100) silicon," *Elec. Mater. Conf. Tech. Dig.*, pp. 22–23, 1992.

[37] D. L. Harame, J. M. C. Stork, B. S. Meyerson, E. F. Crabbe, G. J. Scilla, E. de Fresart, A. E. Megdanis, C. L. Stanis, G. L. Patton, A. A. Bright, J. B. Johnson, and S. S. Furkay, " 30GHz polysilicon-emitter and singe-crystal-emitter graded SiGe-base PNP transistors," *International Electron Devices Meeting Tech. Dig.*, pp. 33–36, 1990.

[38] H. F. Cooke, "Microwave transistors: Theory and design," *Proc. IEEE*, vol. 59, pp. 1163–1181, 1971.

[39] H. Kroemer, "Two integral relationships pertaining to the electron transport through a bipolar transistor with a nonuniform energy gap in the base region," *Solid-State Electron.*, vol. 28, pp. 1101–1103, 1985.

[40] T. Y. Chiu, G. M. Chin, M. Y. Lau, R. C. Hanson, M. D. Morris, K. F. Lee, T. Y. M. Liu, A. M. Voschenkov, R. G. Schwartz, V. D. Archer, S. N. Finegan, and M. D. Feuer, "The design and characterization of Nonoverlapping Super Self-aligned BiCMOS technology," *IEEE Trans. Electron Devices*, vol. 38, pp. 141–150, 1991.

[41] D. D. Tang and P. M. Solomon, "Bipolar transistor design for optimized power-delay logic circuits," *IEEE J. Solid-State Circuits*, vol. 14, pp. 679–684, 1979.

[42] J. M. C. Stork, "Bipolar transistor scaling for minimum switching delay and energy dissipation," *International Electron Devices Meeting Tech. Dig.*, pp. 550–553, 1988.

[43] K. G. Moerschei, T. Y. Chiu, P. W. A, K. S. Lee, R. G. Schwartz, R. A. Mantz, T. Y. M. Liu, K. F. Lee, V. D. Archer, G. R. Hower, G. T. Mazea, R. E. Carsia, J. A. Pavlo, M. P. Ling, J. L. Delein, F. M. Ereeg, J. J. Egan, C. J. Fassi, J. T. Glich, and M. A. Prosnic, "ATT's bipolar process is BEST," *Semiconductor International*, pp. 72–74, Nov. 1990.

[44] T. Y. Chiu, J. M. Sung, and T. M. Liu *private communication*, 1991/92.

[45] T. M. Liu, G. M. Chin, D. Y. Jeon, M. D. Morris, V. D. Archer, H. H. Kom, M. Cerullo, K. F. Lee, J. M. Sung, K. Lau, T. Y. Chiu, A. M. Voschenkov, and R. G. Schwartz, "A half-micron Super Self-aligned BiCMOS Technology for high speed applications," *International Electron Devices Meeting Tech. Dig.*, pp. 23–26, 1992.

[46] E. J. Prinz and J. C. Sturm, "Current gain – Early voltage products in heterojunction bipolar transistors with nonuniform base bandgaps," *IEEE Electron Device Lett.*, vol. 12, pp. 661–663, 1991.

[47] A. Gruhle, "The influence of emitter-base junction design on collector saturation current, ideality factor, Early voltage, and device switching speed of Si/SiGe HBT's," *IEEE Trans. Electron Devices*, vol. 41, pp. 198–203, 1994.

[48] E. J. Prinz, P. M. Garone, P. V. Schwartz, X. Xiao, and J. C. Sturm, "The effect of base emitter spacers and strain-dependent densities of states in $Si/Si_{1-x}Ge_x/Si$ heterojunction bipolar transistors," *International Electron Devices Meeting Tech. Dig.*, pp. 639–642, 1989.

[49] E. J. Prinz, P. M. Garone, P. V. Schwartz, X. Xiao, and J. C. Sturm, "The effects of base dopant outdiffusion and undoped $Si_{1-x}Ge_x$ junction spacer layers in $Si/Si_{1-x}Ge_x/Si$ heterojunction bipolar transistors," *IEEE Electron Device Lett.*, vol. 12, pp. 42–44, 1991.

[50] J. W. Slotboom, G. Streutker, A. Pruijmboom, and D. J. Gravesteijn, "Parasitic energy barriers in SiGe HBT's," *IEEE Electron Device Lett.*, vol. 12, pp. 486–488, 1991.

[51] D. D. Tang and P.-F. Lu, "A reduced-field design concept for high-performance bipolar transistors," *IEEE Electron Device Lett.*, vol. 10, pp. 67–69, 1989.

[52] D. C. D'Avanzo, M. Vanzi, and R. W. Dutton, "One-dimensional semiconductor device analysis (SEDAN)," *Stanford Univ. Tech. Rep. G-201-5*, vol. Stanford, CA, Oct. 1979.

[53] P. Kuo, J. L. Hoyt, J. F. Bibbons, J. E. Turner, R. D. Jacowitz, and T. I. Kamins, "Comparison of boron diffusion in Si and strained $Si_{1-x}Ge_x$ epitaxial layers," *Appl. Phys. Lett.*, vol. 62, pp. 612–614, 1993.

[54] N. Moriya, L. C. Feldman, H. S. Luftman, C. A. King, J. Bevk, and B. Freer, "Boron diffusion strained $Si_{1-x}Ge_x$ epitaxial layers," *Phys. Rev. Lett.*, vol. 62, pp. 883–886, 1993.

[55] S. M. Hu, "Diffusion and segregation in inhomogeneous media and the $Si_{1-x}Ge_x$ heterostructure," *Phys. Rev. Lett.*, vol. 63, pp. 2492–2495, 1989.

[56] S. M. Hu, D. C. Ahlgren, P. A. Ronsheim, and J. O. Chu, "Experimental study of diffusion and segregation in a $Si_{1-x}Ge_x$ heterostructure," *Phys. Rev. Lett.*, vol. 67, pp. 1450–1453, 1991.

[57] B. S. Meyerson, "Low-temperature silicon epitaxy by ultrahigh vacuum chemical vapor deposition," *Appl. Phys. Lett.*, vol. 48, pp. 797–799, 1986.

[58] B. S. Meyerson, K. J. Uram, and F. K. LeGoues, "Cooperative phenomena in silicon/germanium low temperature epitaxy," *Appl. Phys. Lett.*, vol. 53, pp. 2555–2557, 1988.

[59] C. M. Gronet, C. A. King, W. Opyd, J. F. Gibbons, S. D. Wilson, and R. Hull, "Growth of $Si/Si_{1-x}Ge_x$ strained-layer superlattices using limited reaction processing," *J. Appl. Phys.*, vol. 61, pp. 2407–2409, 1987.

[60] J. C. Sturm, P. V. Schwartz, E. J. Prinz, and H. Manoharan, "Growth of $Si_{1-x}Ge_x$ by rapid thermal chemical vapor deposition and application to heterojunction bipolar transistors," *J. Vac. Sci. Technol. B*, vol. 9, pp. 2011–2016, 1991.

[61] W. B. de Boer and D. J. Meyer, "Low temperature chemical vapor deposition of epitaxial Si and SiGe layers at atmospheric pressure," *Appl. Phys. Lett.*, vol. 58, pp. 1286–1288, 1991.

[62] P. D. Agnello, T. O. Sedgwick, M. S. Goorsky, J. Ott, T. S. Kuan, G. Scilla, and V. P. Kesan, "Growth of silicon-germanium alloys by atmospheric-pressure chemical vapor deposition at low temperatures," *Mat. Res. Soc. Symp. Proc.*, vol. 220, pp. 607–612, 1991.

[63] J. C. Sturm, P. V. Schwartz, and P. M. Garone, "Silicon temperature measurement by infrared transmission for rapid thermal processing applications," *Appl. Phys. Lett.*, vol. 56, pp. 961–963, 1990.

[64] D. Gräf, M. Grundner, and R. Schulz, "Oxidation of HF-treated Si wafer surfaces in air," *J. Appl. Phys.*, vol. 68, pp. 5155–5161, 1990.

[65] J. C. Sturm, H. Manoharan, L. C. Lenchyshyn, M. L. W. Thewalt, N. L. Rowell, J. P. Noel, and D. C. Houghton, "Well resolved band-edge photoluminescence of excitons confined in strained $Si_{1-x}Ge_x$ quantum wells," *Phys. Rev. Lett.*, vol. 66, pp. 1362–1365, 1991.

[66] E. Chason and D. T. Warwick, "X-ray reflectivity measurements of surface roughness using energy dispersive detection," *Mat. Res. Sump. Proc.*, vol. 208, pp. 351–356, 1991.

[67] E. Chason, T. M. Mayer, A. Payne, and D. Wu, "*in situ* energy dispersive x-ray reflectivity measurement of H ion bombardment on SiO_2/Si and Si," *Appl. Phys. Lett.*, vol. 60, pp. 2353–2355, 1992.

[68] E. Chason and T. M. Mayer, "Low energy bombardment induced roughening and smoothing of SiO_2 surfaces," *Appl. Phys. Lett.*, vol. 62, pp. 363–365, 1993.

[69] D. Dutarte, P. Warren, F. Provenier, F. Chollet, and A. Perio, "Fabrication of relaxed $Si_{1-x}Ge_x$ layers on si substrates by RTCVD," *J. Vac. Sci. Technol. B*, to be published, 1994.

[70] A. J. Pidduck, D. J. Robbins, A. G. Cullis, W. Y. Leong, and A. M. Pitt, "Evolution of surface morphology and strain during SiGe epitaxy," *Thin Solid Films*, vol. 222, pp. 78–84, 1992.

[71] D. Dutarte, P. Warren, I. Berbezier, and P. Perret, "Low temperature Si and $Si_{1-x}Ge_x$ epitaxy by rapid thermal chemical vapour deposition using hydrides," *Thin Solid Films*, vol. 222, pp. 52–56, 1992.

[72] H. C. Liu, D. Landheer, M. Buchanan, and D. C. Houghton, "Resonant tunneling in Si/$Si_{1-x}Ge_x$/Si double-barrier structures," *Appl. Phys. Lett.*, vol. 52, pp. 1809–1811, 1988.

[73] S. S. Rhee, J. S. Park, R. P. G. Karunasiri, Q. Ye, and K. L. Wang, "Resonant tunneling through a Si/GeSi/Si heterostructure on a GeSi buffer layer," *Appl. Phys. Lett.*, vol. 53, pp. 204–206, 1988.

[74] U. Gennser, V. P. Kesan, S. S. Iyer, T. J. Bucelot, and E. S. Yang, "Resonant tunneling of holes through silicon barriers," *J. Vac. Sci. Technol. B*, vol. 8, pp. 210–213, 1990.

[75] K. Ismail, B. S. Meyerson, and P. J. Wang, "Electron resonant tunneling in Si/SiGe double barrier diodes," *Appl. Phys. Lett.*, vol. 59, pp. 973–975, 1991.

[76] Ž . Matutinović Krstelj, C. W. Liu, X. Xiao, and J. C. Sturm, "Symmetric Si/$Si_{1-x}Ge_x$/Si electron resonant tuneling diodes with an anomalous temperature behaviour," *Appl. Phys. Lett.*, vol. 62, pp. 603–605, 1993.

[77] H. C. Manoharan, "Structural and electronic properties of RTCVD-grown strained layer silicon-germanium heterostructures," *Senior Independent Work, Princeton Univ. Princeton, NJ.*, 1991.

[78] J. A. D. Alamo and R. M. Swanson, "Forward-bias tunneling: A limitation to bipolar device scaling," *IEEE Electron Device Lett.*, vol. 7, pp. 629–631, 1986.

[79] J. M. C. Stork and R. D. Isaac, "Tunneling in base-emitter junctions," *IEEE Trans. Electron Devices*, vol. 30, pp. 1527–1534, 1983.

[80] E. Hackbarth and D. D.-L. Tang, "Inherent and stress-induces leakage in heavily doped silicon junctions," *IEEE Trans. Electron Devices*, vol. 35, pp. 2108–2118, 1988.

[81] E. Hackbarth and T.-C. Chen, "Indetification and implication of a perimeter tunneling current component in advance self-aligned bipolar transistors," *IEEE Trans. Electron Devices*, vol. 35, pp. 89–95, 1988.

[82] A. G. Chynoweth, W. L. Feldmann, and R. A. Logan, "Excess tunnel current in silicon Esaki junction," *Phys. Rev.*, vol. 121, pp. 684–694, 1961.

[83] Ž. Matutinović-Krstelj, E. J. Prinz, P. V. Schwartz, and J. C. Sturm, "Reduction of the p^+-n^+ junction tunneling current for base current improvement in Si/SiGe/Si heterojunction bipolar transistors," *IEEE Electron Device Lett.*, vol. 12, pp. 163–165, 1991.

[84] J. del Alamo, S. Swirhun, and R. M. Swanson, "Simultaneous measurement of hole lifetime, hole mobility and bandgap narrowing in heavily doped n-type silicon," *International Electron Devices Meeting Tech. Dig.*, 1985.

[85] S. Swirhun, Y.-H. Kwark, and R. M. Swanson, "Measurement of electron lifetime, electron mobility and bandgap narrowing in heavily doped p-type Silicon," *International Electron Devices Meeting Tech. Dig.*, 1986.

[86] S. M. Sze, *Physics of semiconductor devices.* John Wiley & Sons, New York, NY, 1981.

[87] J. H. Comfort, E. F. Crabbe, J. D. Cressler, W. Lee, J. Y.-C. Sun, J. Malinowski, M. D'Agostino, J. N. Burghartz, J. M. C. Stork, and B. S. Meyerson, "Single crystal emitter cap for epitaxial Si- and SiGe-base transistors," *International Electron Devices Meeting Tech. Dig.*, pp. 857–860, 1991.

[88] M. Ghannam and R. Mertens, "Accurate determination of bandgap narrowing in heavily-doped epitaxial p-type silicon," *Microelectronic Engineering*, vol. 19, 1992.

[89] D. Klaassen, J. Slotboom, and H. de Graaff, "Unified apparent bandgap narrowing in n- and p-type Silicon," *Solid-State Electronics*, vol. 35, 1992.

[90] A. Pruijmboom, C. E. Timmering, J. M. L. van Rooij-Mulder, D. J. Gravesteijn, W. B. de Boer, W. J. Kersten, J. W. Slotboom, C. J. Vriezema, and R. de Kruif,

"Heterojunction bipolar transistors with SiGe base," *Microelectronic Engineering*, vol. 19, pp. 427–434, 1992.

[91] P. Narozny, H. Dämkes, H. Kibbel, and E. Kasper, "Si/SiGe heterojunction bipolar transistors made by molecular beam epitaxy," *IEEE Trans. Electron Devices*, vol. 36, pp. 2363–2366, 1989.

[92] T. Manku and A. Nathan, "Effective mass for strained p-type $Si_{1-x}Ge_x$," *J. Appl. Phys.*, vol. 69, pp. 8414–8416, 1991.

[93] T. Manku and A. Nathan, "Lattice mobilty of holes in strained and unstrained $Si_{1-x}Ge_x$ alloys," *IEEE Electron Device Lett.*, vol. 12, pp. 704–706, 1991.

[94] T. Manku, J. M. McGregor, A. Nathan, D. J. Roulston, J.-P. Noel, and D. C. Houghton, "Drift hole mobilty in strained and unstrained doped $Si_{1-x}Ge_x$ alloys," *IEEE Trans. Electron Devices*, vol. 40, pp. 1990–1995, 1993.

[95] J. M. McGregor, T. Manku, J.-P. Noel, D. J. Roulston, A. Nathan, and D. C. Houghton, "Measured in-plane hole drift and hall mobilty in heavily-doped strained p-type $Si_{1-x}Ge_x$," *J. Electron. Materials*, vol. 22, pp. 319–421, 1993.

[96] J. del Alamo, "Minority carrier trasnsport in heavily doped n-type silicon," *Ph.D. dissertation, Stanford Univ. Stanford, Ca.*, 1985.

[97] S. E. Swirhun, "Characterization of majority and minority carrier transport in heavily doped silicon," *Ph.D. dissertation, Stanford Univ. Stanford, Ca.*, 1987.

[98] J. Poortmans, S. C. Jain, M. Caymax, A. V. Ammel, J. Nijs, R. P. Mertens, and R. V. Overstraeten, "Evidence of the influence of heavy doping induced bandgap narrowing on the collector current of strained SiGe-base HBT's," *Microelectronic Engineering*, vol. 19, 1992.

[99] J. C. Sturm, E. J. Prinz, P. M. Garone, and P. V. Schwartz, "Band-gap shifts in silicon-germanium heterojunction bipolar transistors," *Appl. Phys. Lett.*, vol. 54, pp. 2707–2709, 1989.

[100] J. C. Sturm and E. J. Prinz, "Graded base $Si/Si_{1-x}Ge_x/Si$ heterojunction bipolar transistors grown by rapid thermal chemical vapor deposition with near-ideal electrical characteristics," *IEEE Electron Device Lett.*, vol. 12, pp. 303–305, 1991.

[101] S. Swirhun, D. Kane, and R.M.Swanson, "Temperature dependence of minority electron mobility and bandgap narrowing in p^+ Si," *International Electron Devices Meeting Tech. Dig.*, 1988.

[102] T. Manku and A. Nathan, "Energy band structure for strained p-type $Si_{1-x}Ge_x$," *Phys. Rev. B*, vol. 43, pp. 12634–12637, 1991.

[103] L. E. Kay and T.-W. Wang, "Monte carlo calculation of strained and unstrained electron mobilities in $Si_{1-x}Ge_x$ using an improved ionized-impurity model," *J. Appl. Phys.*, vol. 70, pp. 1483–1488, 1991.

[104] G. E. Possin, M. S. Adler, and B. J. Baliga, "Measurements of the p-n product in heavily doped epitaxial emitters," *IEEE Trans. Electron Devices*, vol. 31, pp. 3–17, 1984.

[105] S. Jain and D. Roulston, "A simple expression for bandgap narrowing in heavily doped Si, Ge, GaAs and GeSi strained layers," *Solid-State Electronics*, vol. 34, 1991.

[106] J. Wagner, "Bandgap narrowing in heavily doped silicon at 20 and 300K studied by photoluminescence," *Phys. Rev. B*, vol. 32, 1985.

[107] W. P. Dumke, "Bandgap narrowing from luminescence in p-type Si," *J. Appl. Phys.*, vol. 54, 1983.

[108] Ž. Matutinović Krstelj, V. Venkataraman, E. J. Prinz, and J. C. Sturm, "A comprehensive study of lateral and vertical current transport in $Si/Si_{1-x}Ge_x/Si$ HBT's," *International Electron Devices Meeting Tech. Dig.*, pp. 87–90, 1993.

[109] A. Wieder, "Emitter effects in shallow bipolar device: measurements and consequences," *IEEE Trans. Electron Devices*, vol. 54, 1983.

[110] J. D. Beck and R. Conradt, "Auger-recombination in Si," *Solid-St.Comm.*, 1973.

[111] J. Dziewior and W. Schmid, "Auger coefficients for highly doped and highly excited silicon," *Appl. Phys. Lett.*, vol. 31, 1977.

[112] D. T. Stevenson and R. J. Keyes, "Measurements of carrier lifetime in germanium and silicon," *J. Appl. Phys.*, vol. 26, pp. 190–195, 1955.

[113] J. Dziewior and D. Silber, "Minority carrier diffusion coefficients in highly doped silicon," *Appl. Phys. Lett.*, vol. 35, 1979.

[114] K. Misiakos, C. H. Wang, and A. Neugroshel, "Method for simultaneus measurement of diffusivity, lifetime, and diffusion length, with application to heavily doped silicon," *IEEE Electron Device Lett.*, vol. 10, 1989.

[115] W. D. Eades, "Characterization of silicon-silicon dioxide interface traps using deep level transient spectroscopy," *Ph.D. dissertation, Stanford Univ. Stanford, Ca.*, 1985.

[116] K. Misiakos, C. H. Wang, A. Neugroshel, and F. A. Lindholm, "Simultaneus extraction of minority carrier transport parameters in crystalline semiconductors by lateral photocurrent," *J. Appl. Phys.*, vol. 67, 1990.

[117] T. E. Haynes and O. W. Holland, "Production of lattice damage during ion implantation of SiGe alloys," *Elec. Mater. Conf. Tech. Dig.*, p. 50, 1992.

[118] I. Y. Leu and A. Neugroshel, "Minority carrier transport parameters in heavily doped p-type silicon at 296 and 77K," *IEEE Trans. Electron Devices*, vol. 40, 1993.

[119] J. C. Sturm, A. S. Amour, Q. Mi, L. C. Lenchyshyn, and M. L. W. Thewalt, "High temperature (77-300K) photo- and electroluminescence in $Si/Si_{1-x}Ge_x$ heterostructures," *Jpn. J. Appl. Phys.*, vol. 33, to be published 1994.

[120] T. Sollner, W. D. Goodhue, P. E. Parker, and D. D. Peck, "Resonant tunneling through quantum wells at frequencies up to 2.5 THz," *Appl. Phys. Lett.*, vol. 43, pp. 588–590, 1983.

[121] S. Luryi, "Frequency limit of double-barrier resonant-tunneling oscillators," *Appl. Phys. Lett.*, vol. 47, pp. 490–492, 1985.

[122] N. C. Kluksdahl, A. Kriman, D. K. Ferry, and C. Ringhofer, "Transient switching behavior of the resonant-tunneling diode," *IEEE Electron Device Lett.*, vol. 9, pp. 457–459, 1988.

[123] F. Capasso, S. Sen, A. C. Gossard, A. Hutchinson, and J. English, "Quantum-well resonant tuneling bipolar transistor operating at room temperature," *IEEE Electron Device Lett.*, vol. 7, pp. 573–576, 1986.

[124] S. Sen, F. Capasso, A. Y. Cho, and D. L. Sivco, "Resonant tuneling device with multiple negative differential resistance: digital and signal processing applications with reduced circuit complexity," *IEEE Trans. Electron Devices*, vol. 34, pp. 2185–2192, 1987.

[125] T. Tanoue, H. Mizuta, and S. Takahashi, "A triple-well resonant tuneling diode for multiple valued logic applications," *IEEE Electron Device Lett.*, vol. 9, pp. 365–368, 1988.

[126] S. Sen, F. Capasso, A. Y. Cho, and D. L. Sivco, "Parity generator circuit using a multi-state resonant tuneling bipolar transistor," *Electronics Lett.*, vol. 24, pp. 1506–1510, 1988.

[127] S. Sen, F. Capasso, A. Y. Cho, and D. L. Sivco, "Multiple state resonant tuneling bipolar transistor operating at room temperature and its application as a frequency multiplier," *IEEE Electron Device Lett.*, vol. 9, pp. 533–536, 1988.

[128] Ž. Matutinović-Krstelj, C. W. Liu, X. Xiao, and J. C. Sturm, "Symmetric $Si/Si_{1-x}Ge_x/Si$ electron resonant tunneling diodes with an anomalous temperature behavior," *Appl. Phys. Lett.*, vol. 62, pp. 603–605, 1993.

[129] S.-Y. Lin *private communication*, 1992.

[130] A. Zaslavsky, "Double barrier resonant tunneling in three and two dimensions," *Ph.D. dissertation, Princeton Univ. Princeton, NJ.*, 1991.

[131] Ž. Matutinović-Krstelj, C. W. Liu, X. Xiao, and J. C. Sturm, "Evidence of phonon-absorption-assisted ssige electron resonant tunneling in $Si/Si_{1-x}Ge_x/Si$ diodes," *J. Vac. Sci. Technol. B*, vol. 11, pp. 1145–1148, 1993.

[132] V. J. Goldman, D. C. Tsui, and J. E. Cunningham, "Evidence of LO-phonon-emission-assisted tuneling in double-barrier heterostructures," *Phys. Rev. B*, vol. 36, pp. 7635–7637, 1987.